






# Local Motion and Contrast Priors Driven Deep Network for Infrared Small Target Superresolution

Xinyi Ying , Yingqian Wang , Longguang Wang , Weidong Sheng , Li Liu , *Senior Member, IEEE*,  
Zaiping Lin, and Shilin Zhou

**Abstract**—Infrared small target superresolution (SR) aims to recover a reliable and detailed high-resolution image with high-contrast targets from its low-resolution counterparts. Since the infrared small target lacks color and fine structure information, it is significant to exploit the supplementary information among sequence images to enhance the target. In this article, we propose the first infrared small target SR method named local motion and contrast prior driven deep network (MoCoPnet) to integrate the domain knowledge of the infrared small target into deep network, which can mitigate the intrinsic feature scarcity of infrared small targets. Specifically, motivated by the local motion prior in the spatio-temporal dimension, we propose a local spatio-temporal attention module to perform implicit frame alignment and incorporate the local spatio-temporal information to enhance the local features (especially for small targets). Motivated by the local contrast prior in the spatial dimension, we propose a central difference residual group to incorporate the central difference convolution into the feature extraction backbone, which can achieve center-oriented gradient-aware feature extraction to further improve the target contrast. Extensive experiments have demonstrated that our method can recover accurate spatial dependence and improve the target contrast. Comparative results show that the MoCoPnet can outperform the state-of-the-art video SR and single image SR methods in terms of both SR performance and target enhancement. Based on the SR results, we further investigate the influence of SR on infrared small target detection and the experimental results demonstrate that the MoCoPnet promotes the detection performance.

**Index Terms**—Attention, central difference convolution (CD-Conv), infrared small target superresolution (SR).

## I. INTRODUCTION

**I**NFRARED imaging system is all-weather in day and night and has high penetrability, sensitivity, and concealment. Infrared imaging system is widely used in security monitoring,

Manuscript received 14 January 2022; revised 23 March 2022 and 17 May 2022; accepted 12 June 2022. Date of publication 15 June 2022; date of current version 20 July 2022. This work was supported in part by the National Key Research and Development Program of China under Grant 2021YFB3100800, and in part by the National Natural Science Foundation of China under Grant 61872379. (Corresponding authors: Zaiping Lin; Li Liu.)

Xinyi Ying, Yingqian Wang, Longguang Wang, Weidong Sheng, Zaiping Lin, and Shilin Zhou are with the College of Electronic Science and Technology, National University of Defense Technology, Changsha 410073, China (e-mail: yingxinyi18@nudt.edu.cn; wangyingqian16@nudt.edu.cn; wanglongguang15@nudt.edu.cn; shengweidong1111@sohu.com; linzaiping@sina.com; zhoushilin@nudt.edu.cn).

Li Liu is with the College of System Engineering, National University of Defense Technology, Changsha 410073, China (e-mail: dreamliu2010@gmail.com).

The code is available at <https://github.com/XinyiYing/MoCoPnet>.  
Digital Object Identifier 10.1109/JSTARS.2022.3183230

remote sensing investigation, aerospace offense-defense, and other military mission. Recently, low-resolution (LR) infrared images cannot meet the high requirements of practical military mission. Therefore, it is necessary to improve the resolution of infrared images. A straightforward way to obtain high-resolution (HR) infrared images is to increase the size of infrared sensor arrays. However, due to the technical limitations of sensors and the high cost of large infrared sensor arrays, it is necessary and important to develop practical, low cost, and highly reliable infrared image superresolution (SR) algorithms. Note that, modern autonomous driving technology requires the infrared imaging system to detect the target in a fairly long distance. Therefore, the target only occupies a very small proportion of the whole image, and is susceptible to noise and clutters. In this article, we mainly focus on infrared small target SR task and investigate its influence on infrared small target detection.

The special imaging mechanism and military application of the infrared imaging system put forward the following requirements for infrared small target SR.

- 1) *High fidelity of superresolved images.* Noise and false contours should be avoided as much as possible.
- 2) *High contrast of superresolved targets.* The target contrast in the superresolved images should be strengthened to boost the subsequent tasks.
- 3) *High robustness to complex scenes and noise.* Small objects are sometimes submerged in clutter, and thus, of low local contrast to the background. SR algorithms should be robust to various complex scenes and imaging noise.
- 4) *High generalization to insufficient datasets.* The lack of infrared image datasets requires that SR algorithms should achieve stable results with a relative small dataset.

The motivations of our method come from data analysis, and can be summarized as follows.

- 1) The target occupies a small proportion of the whole infrared image (generally less than 0.12% [1]) and lacks color and fine structure information (e.g., contour, shape, and texture). Few information is available for SR within a single image. Therefore, we perform SR on image sequences to use the supplementary information among the temporal dimension to improve the SR performance and the target contrast.
- 2) Due to the long distance between the target and the imaging system, the mobility of the targets on the imaging plane is limited, leading to small motion of the target

between neighborhood frames (*i.e.*, local motion prior [2], [3] in spatio-temporal dimension). Therefore, we design a local spatio-temporal attention (LSTA) module to perform implicit frame alignment and exploit the supplementary information in the local spatio-temporal neighborhood to enhance the local features (especially for small targets).

- 3) Compared with the background clutter, the contrast and gradient between the target and the background in the local neighborhood are high in all directions (*i.e.*, local contrast prior [4], [5] in spatial dimension). Therefore, we design a center difference residual group (CD-RG) to achieve center-oriented gradient-aware feature extraction, which can encode the local contrast prior to further improve the target contrast.

Based on the aforementioned observations, we propose a local motion and contrast prior driven deep network (MoCoPnet) for infrared small target SR. The main contributions can be summarized as follows.

- 1) We propose the first infrared small target SR method named MoCoPnet and summarize the definition and requirements of this task. The proposed modules (*i.e.*, CD-RG and LSTA module) of the MoCoPnet integrate the domain knowledge (*i.e.*, local contrast prior and local motion prior) of infrared small targets into deep networks, which can mitigate the intrinsic feature scarcity of data-driven approaches [5].
- 2) The experimental results demonstrate that the MoCoPnet can achieve state-of-the-art SR performance and effectively improve the target contrast.
- 3) Based on the SR results, we further investigate the influence of SR on infrared small target detection. The experimental results show that the MoCoPnet can promote the detection performance to achieve a high signal-to-noise ratio gain (SNRG), signal-to-clutter ratio gain (SCRG), contrast gain (CG) scores, and improved receiver operating characteristic curve (ROC) results.

## II. RELATED WORK

### A. Single Image SR

Image SR is an inherently ill-posed optimization problem and has been investigated for decades. In literature, researchers have proposed a variety of classic single image SR (SISR) methods, including prediction-based methods [6], [7], edge-based methods [8], [9], statistics-based methods [10], [11], patch-based methods [9], [12], and sparse representation methods [13], [14]. However, most of the aforementioned traditional methods use handicraft features to reconstruct HR images, which cannot formulate the complex SR process, and thus, limits the SR performance. Recently, due to the powerful feature representation capability, convolutional neural networks (CNNs) have been widely used in single image SR task and achieve the state-of-the-art performance [15], [16]. Dong *et al.* [17] proposed the pioneering CNN-based work SRCNN to recover an HR image from its LR counterpart. Kim *et al.* [18] deepened the network to 20 convolutional layers (*i.e.*, VDSR) and achieved improved SR performance by increasing model complexity.

Moreover, various increasingly deep and complex architectures (*e.g.*, residual networks [19], recursive networks [20]–[23], densely connected networks [24]–[26], and attention-based networks [15], [27]) have also been applied to SISR for performance improvement. Other than tackling image average distortion by norm loss, generative adversarial image SR networks [28], [29] employed the perceptual loss for perceptual quality improvement.

### B. Video SR

Existing video SR methods commonly follow a three-step pipeline, including feature extraction, motion compensation, and reconstruction [30]. Traditional video SR methods [31], [32] employ handcrafted models to estimate motion, noise, and blur kernel and reconstruct HR video sequences. Recent deep learning-based video SR methods are better in exploiting spatio-temporal information by its powerful feature representation capability and can achieve the state-of-the-art performance. Liao *et al.* [33] proposed the pioneering CNN-based video SR method to perform motion compensation by optical flow, and then, ensembled the compensated drafts via CNN. Afterwards, a series of optical flow-based video SR algorithms [34], [35] emerged to explicitly perform motion estimation and frame alignment, resulting in vague and duplication [36]. To avoid the aforementioned problem, deformable convolution [37], [38] has been employed to perform motion compensation explicitly in a unified step [39], [40] through extra offsets. Apart from these explicit motion compensation methods, implicit approaches (*e.g.*, 3-D convolution networks [41], [42], recursive networks [43], [44], and nonlocal networks [40], [45]) have also been applied to video SR for performance improvement.

### C. Infrared Image SR

With the increased demands of high-resolution infrared images, some researchers perform image SR on infrared images. Traditional methods [46] consider SR as sparse signal reconstruction in compressive sensing. Based on the previous studies, Zhang *et al.* [47] combined compressive sensing and deep learning to achieve an improved SR performance with low computational cost. Han *et al.* [48] proposed to employ CNNs to recover high-frequency components with upscaled LR images to generate the SR results. He *et al.* [49] proposed a cascaded deep network with multiple receptive fields for large scale factor ( $\times 8$ ) infrared image SR. Liu *et al.* [50] proposed to use a generative adversarial network and perceptual loss to reconstruct the texture details of infrared images. Chen *et al.* [51] employed an iterative error reconstruction mechanism to perform SR in a coarse-to-fine manner. Huang *et al.* [52] proposed a progressive SR generative adversarial network and employed the multistage transfer learning strategy to improve the SR performance from small samples. Prajapati *et al.* [53] proposed a channel splitting-based CNN to eliminate the redundant features for efficient inference. Yang *et al.* [54] proposed a visible-assisted training strategy to promote details preservation.

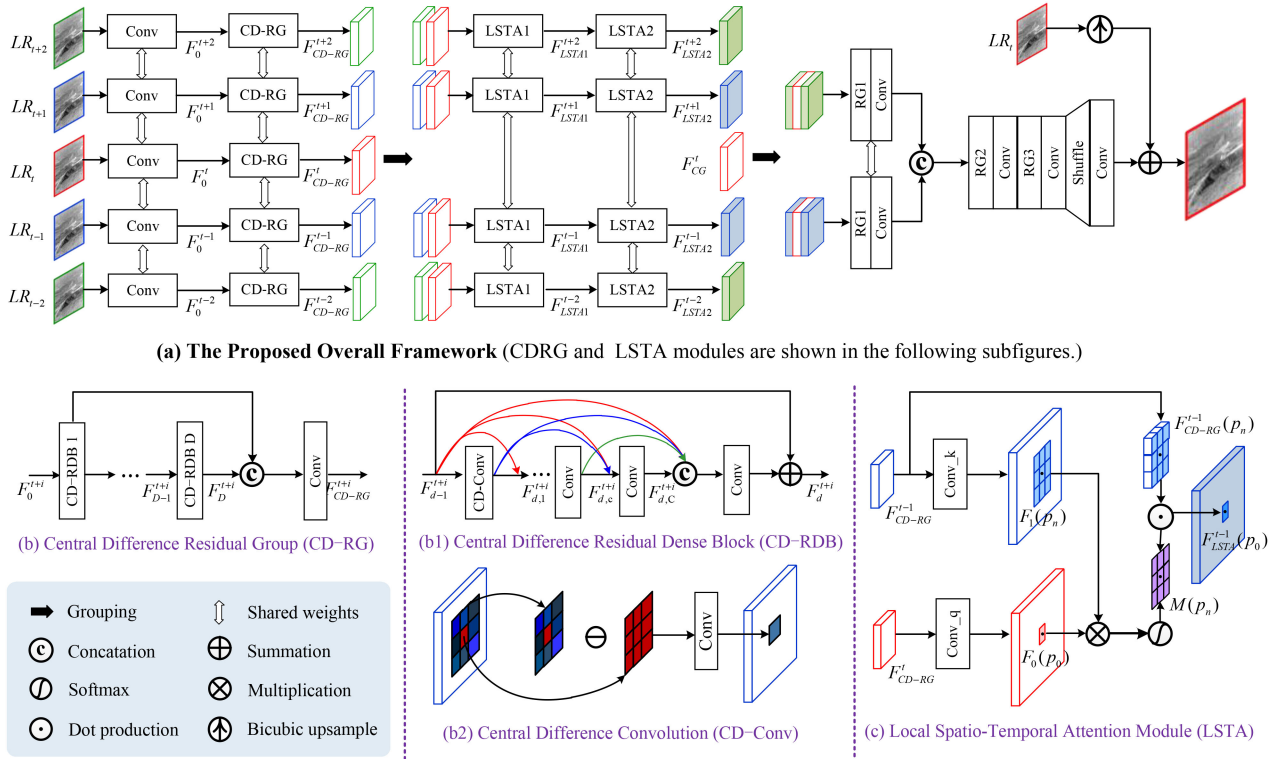


Fig. 1. Proposed architecture of the MoCoPnet. (a) Overall framework. (b) CD-RG, and (b1) and (b2) its submodules central difference dense block (CD-RDB) and CD-Conv, respectively. (c) LSTA module with kernel size 3 and dilation rate 1.

#### D. Attention Mechanism

Since the importance of each spatial location and channel is not uniform, Hu *et al.* [55] proposed SeNet for classification, which consists of selection units to control the switch of passed data. Zhang *et al.* [15] proposed a channel attention mechanism to calculate the importance along the channel dimension for channel selection. Anwar *et al.* [56] proposed feature attention to urge the network to pay more attention to the high-frequency region. Dai *et al.* [27] proposed second-order attention to adaptively readjust features for powerful feature correlation learning. Wang *et al.* [57] explored the sparsity in SR task and proposed sparse masks for efficient inference. The spatial mask and channel mask calculate the importance along both the spatial dimension and the channel dimension to prune the redundant computations. The aforementioned studies only consider the global importance on spatial and channel dimension. Since small targets only occupy a small portion in the whole image and have a high contrast with the local neighborhood, we design a local attention mechanism that can better characterize the small targets.

#### E. Sequence Image Infrared Small Target Detection

Sequence image infrared small target detection is significant for long-range precision strikes, aerospace offensive-defensive countermeasures, and remote sensing intelligence reconnaissance. According to whether the sequential information is used, sequence image infrared small target detection methods can be divided into two categories: detect before track (DBT) methods and track before detect (TBD) methods. Based on the results of

single image infrared small target detection [5], [58]–[61], DBT methods employed the motion trajectory of targets through sequence image projection to eliminate the false targets and reduce the false alarm rate. DBT methods have a low computational cost and are easy to implement. However, the performance drops rapidly with a low SNR. TBD methods [62]–[64] commonly follow a three-step pipeline, including background suppression, region of interest extraction, and target detection. TBD methods are robust to images with a low SNR but have a high computational cost, which cannot meet the requirements of real-time detection. It is challenging to achieve a high detection rate and low false alarm rate in real time due to the lack of target information, the complex background noise, the insufficient public datasets, and the explosion of data amount and the computational cost. Therefore, it is necessary to recover reliable image details and enhance the contrast between target and background for detection.

### III. METHODOLOGY

In this section, we introduce our method in details. Specifically, Section III-A introduces the overall framework of our network. Sections III-B and III-C introduce the two modules that integrate local contrast prior and local motion prior of infrared small target into deep networks.

#### A. Overall Framework

The overall framework of our MoCoPnet is shown in Fig. 1. Specifically, an image sequence with five frames  $LR_{t+i}$  ( $i =$

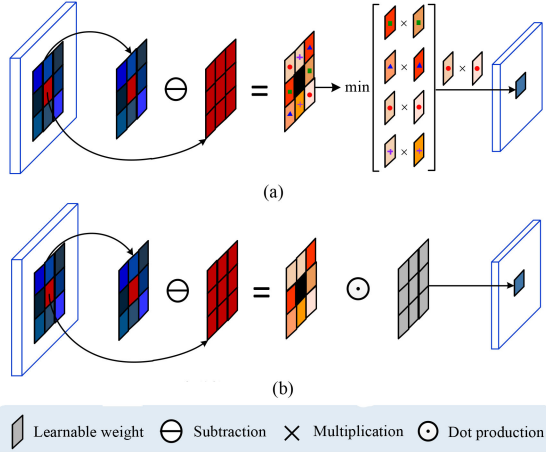


Fig. 2. Differences between (a) DLCM (see [5]) and (b) CD-Conv (see [65] and [66]). (a) Dilated local contrast measure (DLCM). (b) Central difference convolution (CD-Conv).

$[-2, 2]$  is first sent to a convolutional layer to generate the initial features  $F_0^{t+i}$  ( $i = [-2, 2]$ ), which are then sent to the CD-RG to achieve center-oriented gradient-aware feature extraction. Then, each neighborhood feature  $F_{\text{CD-RG}}^{t+i}$  ( $i = -2, -1, 1, 2$ ) is paired with the reference feature  $F_{\text{CD-RG}}^t$  and sent to two LSTA modules to achieve motion compensation and enhance the local features. Next, the reference feature  $F_{\text{CD-RG}}^t$  is concatenated with two compensated neighborhood frames  $F_{\text{LSTA2}}^{t+k}$ ,  $F_{\text{LSTA2}}^{t-k}$  ( $k = 1, 2$ ), and then, sent to a residual group (RG) and a convolution layer for coarse fusion. Afterwards, the two fused features are concatenated and sent to an RG and a convolution for fine fusion. Then, the fused feature is processed by an RG, a subpixel layer and a convolutional layer for SR reconstruction and upsampling. Finally, the SR reference frame is obtained by adding the bicubically upsampled LR reference frame to accelerate the training convergence. Note that, the number of the input frames is set to 7 in this article and the process is the same as in Fig. 1(a). We use the mean square error (MSE) between the SR reference frame and the groundtruth reference frame as the loss function of our network.

### B. Central Difference Residual Group (CD-RG)

The CD-RG incorporates central difference convolution (CD-Conv [65], [66]) into RG (see [15] and [26]) to achieve the center-oriented gradient-aware feature extraction, which can utilize the spatial local salient prior to strengthen the contrast of the small targets. Note that, we employ RG as the backbone of our MoCoPnet for the following reasons: RG can generate features with large receptive field and dense sampling rate, which promotes the information exploitation. The reuse of hierarchical features not only improves the SR performance [67] but also maintains the information of small targets [1], [61], [68].

The architecture of the CD-RG is shown in Fig. 1(b). The input feature  $F_0^{t+i}$  is first fed to  $D$  central difference residual dense blocks (CD-RDB) [26] to extract hierarchical features. Then, the hierarchical features are concatenated and fed to a  $1 \times 1$  convolutional layer to generate output feature  $F_{\text{CD-RG}}^{t+i}$ .

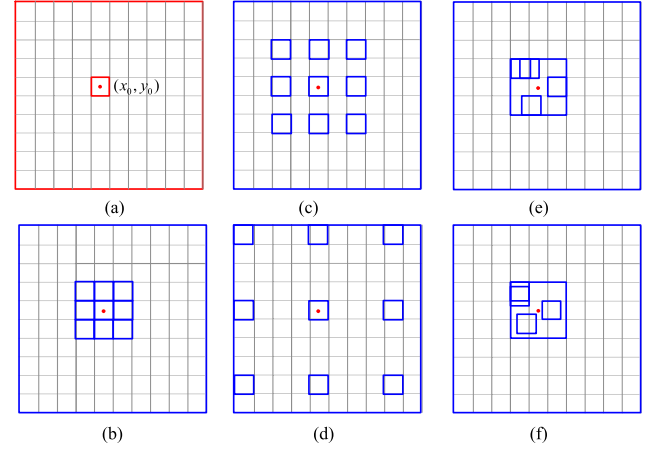


Fig. 3. Illustration of the LSTA module with difference kernel size of kern and dilation rate of dila. (a) Reference frame and pixel  $(x_0, y_0)$  is highlighted by a red box. (b)–(f) Corresponding neighborhood pixels centered in  $(x_0, y_0)$  and are highlighted by blue boxes. (a) Reference frame. (b) STLA(kern=3, dila=1). (c) STLA(kern=3, dila=2). (d) STLA(kern=3, dila=4). (e) STLA(kern=5, dila=1/2). (f) STLA(kern=9, dila=1/4).

As is shown in Fig. 1(b1), 1 CD-Conv and  $K - 1$  Convs with a growth rate of  $G$  are used within each CD-RDB to achieve a dense feature representation. The architecture of CD-Conv is shown in Fig. 1(b2). CD-Conv aggregates the center-oriented gradient information, which echoes the spatial local saliency prior of infrared small target. As shown in Fig. 2, different from handcrafted dilated local contrast measure (DLCM [5]), which can only reserve the contrast information in one direction, CD-Conv is a learnable measure and can improve the contrast of small target while maintaining the background information. In conclusion, CD-Conv is more in line with the task of infrared small target SR (*i.e.*, recovering reliable and detailed high-resolution image with high-contrast target). DLCM and CD-Conv can be formulated as  $f(x, y)$  and  $g(x, y)$  as follows:

$$f(x, y) = \min_{(i,j) \in \Omega^+} \{(S_{x,y} - S_{x-i,y-j})(S_{x,y} - S_{x+i,y+j})\} \quad (1)$$

$$g(x, y) = \sum_{(i,j) \in \Omega} \omega_{i,j} (S_{x+i,y+j} - \theta S_{x,y}) \quad (2)$$

where  $S_{x,y}$  represents the value of a specific location  $(x, y)$  in the feature map, and  $(i, j) \in \Omega^+ = (d, d), (d, 0), (d, -d), (0, d)$  is the direction index.  $\omega_{i,j}$  is a learnable weight to continuously optimize the local contrast measure and  $\theta \in [0, 1]$  is a hyperparameter to balance the contribution between gradient-level detailed information and intensity-level semantic information. Note that,  $\theta$  is set to 0.7 [65] in this article.

### C. LSTA Module

The LSTA module calculates the local response between the neighborhood frame and the reference frame and uses the local spatio-temporal information to enhance the local features of the reference frames. The inputs of LSTA are the reference frame and one neighborhood frame. For a sequence with seven frames, the operation need to be repeated six times. The architecture of LSTA is shown in Fig. 1(c). The red reference

feature  $F_{CD-RG}^t \in \mathbb{R}^{H \times W \times C}$  and the blue neighborhood feature  $F_{CD-RG}^{t-1} \in \mathbb{R}^{H \times W \times C}$  are first fed to  $1 \times 1$  convolutional layers  $conv\_q$  and  $conv\_k$  for dimension compression to generate  $F_0, F_1 \in \mathbb{R}^{H \times W \times C/cr}$ , where  $cr$  is the compression ratio and is set to 8 in this article. The process can be formulated as

$$\begin{aligned} F_0 &= H_{conv\_q}(F_{CD-RG}^t) \\ F_1 &= H_{conv\_k}(F_{CD-RG}^{t-1}) \end{aligned} \quad (3)$$

where  $H_{conv\_k}$  and  $H_{conv\_q}$  represent  $1 \times 1$  convolutions. Then, we calculate the response between each location  $p_0$  in  $F_0$  and the corresponding neighborhood (centered in  $p_0$ ) in  $F_1$ . Afterwards, the response is summed and softmax along the channel dimension to generate the attention map  $M$ . The process is defined as

$$M(p_n) = \text{softmax} \left( \sum_{k=1}^{C/rd} F_0(p_0, k) \cdot F_1(p_n, k) \right) \quad (4)$$

where  $p_n$  represents the  $n$ th value of the local neighborhood centered in  $p_0$  with kernel size of kern and dilation rate of dila. The purple  $3 \times 3$  grid in Fig. 1(c) is the local attention feature map with parameter (kern = 3, dila = 1). Note that, as shown in Fig. 3(c) and (d), dila can be integer larger than 1 to enlarge the receptive field without additional computational cost. As shown in Fig. 3(e) and (f), dila can also be fractional to capture the subpixel motion between frames and we employ bilinear interpolation to generate the exact corresponding values.

Finally, dot production is performed between the local neighborhood feature  $F_{CD-RG}^{t-1}(p_n)$  centered in  $p_0$  and the corresponding attention map  $M(p_n)$  to generate the value of location  $p_0$  in the output feature  $F_{LSTA}^{t-1}(p_0)$ . The process is formulated as

$$F_{LSTA}^{t-1}(p_0) = \sum_{\forall p_n \in G} F_{CD-RG}^{t-1}(p_n) \cdot M(p_n). \quad (5)$$

LSTA first calculates the response between the reference frame and its adjacent frames to generate the attention map, and then, calculates a weighted summation of these frames using the generated attention maps. In this way, the neighborhood frames can be implicitly aligned and the complementary temporal information can be incorporated to enhance the features of small targets.

#### IV. EXPERIMENTS

In this section, we first introduce the experiment settings, and then, conduct ablation studies to validate our method. Next, we compare our network to several state-of-the-art SISR and video SR methods. Finally, we investigate the influence of SR on infrared small target detection.

##### A. Experiment Settings

In this subsection, we sequentially introduce the datasets, the evaluation metrics, the network parameters, and the training details.

1) *Datasets*: Hui *et al.* [69] developed a dataset for detection and tracking of dim-small aircraft infrared targets under

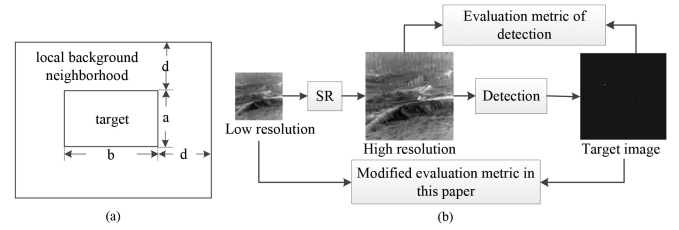


Fig. 4. Evaluation metrics. (a) Local background neighborhood. (b) Modified evaluation metrics in this article.

ground/air background. This dataset contains 22 image sequences (totally 16 177 frames) with a resolution of  $256 \times 256$ . Recently, a large-scale high-quality semisynthetic dataset (named SAITD [70]) has been proposed for small aerial infrared targets detection. SAITD dataset contains 350 image sequences with target annotations and 175 without, 150 185 images in total). The second Anti-UAV Workshop & Challenge (Anti-UAV [71]) releases 250 high-quality infrared video sequences with multiscale UAV targets. In this article, we employ the 1st – 50th sequences with target annotations of SAITD as the test datasets and the remaining 300 sequences as the training datasets. In addition, we employ Hui and Anti-UAV as the test dataset to test the robustness of our MoCoPnet to real scenes. In Anti-UAV dataset, only the sequences with infrared small target [1] (21 sequences in total) are selected as the test set. Note that, we only use the first 100 images of each sequence for test to balance computational/time cost and generalization performance.

2) *Evaluation Metrics*: We employ peak signal-to-noise ratio (PSNR) and structural similarity index (SSIM) to evaluate the SR performance. In addition, we introduce signal-to-noise ratio (SNR) and contrast ratio (CR) in the local background neighborhood [58] of targets to evaluate the performance of recovering small targets. As shown in Fig. 4(a), the size of the target area is  $a \times b$ , and the local background neighborhood is extended from the target area by  $d$  both in width and height. Note that, the parameters of local background neighborhood ( $a, b, d$ ) in HR images are set to (7,7,30), (11,11,50), and (21,21,100) in SAITD,<sup>1</sup> Hui, and Anti-UAV,<sup>2</sup> respectively. When  $4 \times$  SR is performed on HR images, the parameters ( $a, b, d$ ) are set to (29,29,120), (45,45,200), and (85,85,400). When  $4 \times$  down-sampling is performed on HR images, the parameters are set to (3,3,10), (3,3,10), and (5,5,20).

To further evaluate the impact of SR algorithms on infrared small target detection, we adopt SNRG, background suppression factor (BSF), SCRG, CG, and ROC for comprehensive evaluation. Note that, the common detection evaluation metrics calculate the ratio of the statistics in the local background neighborhood before and after detection. Since we first super-resolve the LR image, and then, perform detection, the inputs of detection algorithms, which are the outputs of different SR algorithms, are different. Therefore, direct using the common

<sup>1</sup>The synthetic target size in SAITD is preset to less than  $7 \times 7$ .

<sup>2</sup>The target size is less than 0.12% of the image size [1] (*i.e.*,  $256 \times 256$  in Hui and  $640 \times 512$  in Anti-UAV).

detection evaluation metrics cannot evaluate the impact of SR on detection accurately. To eliminate the influence of different inputs, we modify the first four metrics to calculate the ratio of the statistics in the local background neighborhood between the LR image before SR and the HR target image after detection. The modified evaluation metrics are shown in Fig. 4(b). We then introduce the aforementioned evaluation metrics in details. SNRG is used to measure the SNR improvement of detection algorithms and is formulated as

$$f_{\text{SNRG}} = \frac{\text{SNR}^{\text{out}}}{\text{SNR}^{\text{in}}} = \frac{(P_t/P_b)^{\text{out}}}{(P_t/P_b)^{\text{in}}} \quad (6)$$

where  $[\cdot]^{\text{in}}$  and  $[\cdot]^{\text{out}}$  represent the metrics in the local background neighborhood of the LR images and the HR target images, respectively.  $P_t$  and  $P_b$  are the maximum value of the target area and the background area, respectively. The BSF is used to measure the background suppression effect and is formulated as

$$f_{\text{BSF}} = \frac{\sigma_b^{\text{in}}}{\sigma_b^{\text{out}}} \quad (7)$$

where  $\sigma_b$  is the standard deviation of the background area. The SCRG is used to measure the SCR improvement of detection algorithms and is formulated as

$$f_{\text{SCRG}} = \frac{\text{SCG}^{\text{out}}}{\text{SCG}^{\text{in}}} = \frac{|\mu_t^{\text{out}} - \mu_b^{\text{out}}| / \sigma_b^{\text{out}}}{|\mu_t^{\text{in}} - \mu_b^{\text{in}}| / \sigma_b^{\text{in}}} \quad (8)$$

where  $\mu_t$  and  $\mu_b$  are the mean value of the target area and the background area, respectively. CG is used to measure the improvement of contrast between targets and background and is formulated as

$$f_{\text{CG}} = \frac{\text{CR}_{\text{out}}}{\text{CR}_{\text{in}}} = \frac{|\mu_t^{\text{out}} - \mu_b^{\text{out}}|}{|\mu_t^{\text{in}} - \mu_b^{\text{in}}|}. \quad (9)$$

Note that, in order to avoid the value of ‘‘Inf’’ (*i.e.*, the denominator is zero) and ‘‘NaN’’ (*i.e.*, the numerator and denominator are both zero), we add  $\epsilon$  to each denominator in (6)–(9) to prevent it from being zero.  $\epsilon$  is set to  $1e - 10$  in this article. ROC is used to measure the trend between detection probability  $P_d$  and false alarm probability  $F_a$ , which are formulated as

$$P_d = \frac{\text{TD}}{\text{AT}} \quad (10)$$

$$F_a = \frac{\text{FD}}{\text{NP}} \quad (11)$$

where TD and FD are the number of true detection and false detection. AT and NP are the amount of targets and the number of image pixels. Note that, the criterion for judging true detection is that the distance between the detected location and the groundtruth location is less than threshold  $\tau$  and  $\tau$  is set to 10 pixels [70] in this article.

3) *Network Parameters*: The parameters of CD-RG in the feature extraction is CD-RG ( $D = 4$ ,  $K = 6$ , and  $G = 32$ ) and the parameters of RGs are RG1,2 ( $D = 1$ ,  $K = 4$ ,  $G = 64$ ), RG3 ( $D = 8$ ,  $K = 6$ ,  $G = 32$ ). The parameters of the two LSTAs are LSTA1 (kern = 3, dila = 3) and LSTA2 (kern = 3, dila = 1).

TABLE I  
ABLATION RESULTS OF DLCM, CONV, AND CD-CONV FOR  $4\times$ SR ON SAITD, HUI, AND ANTI-UAV DATASETS

Dataset	Variants	PSNR	SSIM	SNR	CR
SAITD	DLCM	26.37	0.725	0.664	14.200
	Conv	27.92	0.798	<b>0.678</b>	14.250
	CD-Conv	<b>28.17</b>	<b>0.807</b>	<b>0.678</b>	<b>14.259</b>
Hui	DLCM	32.32	0.832	0.820	15.167
	Conv	33.00	0.854	0.846	15.198
	CD-Conv	<b>33.12</b>	<b>0.857</b>	<b>0.859</b>	<b>15.203</b>
Anti-UAV	DLCM	31.44	0.901	0.946	6.739
	Conv	<b>31.85</b>	0.913	0.960	6.696
	CD-Conv	<b>31.85</b>	<b>0.914</b>	<b>0.965</b>	<b>6.709</b>
Avg.	DLCM	30.04	0.820	0.810	12.035
	Conv	30.93	0.855	0.828	12.048
	CD-Conv	<b>31.05</b>	<b>0.859</b>	<b>0.834</b>	<b>12.057</b>

Best results are shown in boldface.

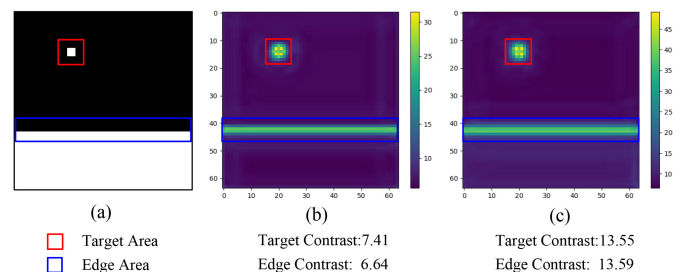


Fig. 5. Toy example of features generated by (b) RG and (c) CD-RG. Note that, (a) represents the corresponding frame of the input image sequence. Red and blue boxes represent target and edge area, and the remaining area is background area. (a) Images. (b) Features after RG. (c) Features after CD-RG.

4) *Training Details*: During the training phase, we randomly extracted seven consecutive frames from an LR video clip, and randomly cropped a  $64 \times 64$  patch as the input. Meanwhile, its corresponding patch in HR video clip was cropped as groundtruth. We followed [35] to augment the training data by random flipping and rotation.

All experiments were implemented on a PC with an Nvidia RTX 3090 GPU. The networks were optimized using the Adam method [72] with  $\lambda_1 = 0.9$  and  $\lambda_2 = 0.999$  and the batch size was set to 12. The learning rate was initially set to  $1e - 3$  and halved in 10 K, 20 K, and 60 K iterations. We trained our network from scratch for 100 K iterations.

## B. Ablation Study

In this subsection, we conduct ablation experiments to validate our design choice.

1) *Central Difference Residual Group (CD-RG)*: To demonstrate the effectiveness of our CD-RG, we replace all the CD-Convs in CD-RG by Convs (*i.e.*, residual group) and retrain the network from scratch. The experimental results in Table I show that CD-RG (*i.e.*, CD-Convs) can introduce 0.12 dB/0.004 gains on PSNR/SSIM and 0.06/0.09 gains on SNR/CR. This demonstrates that CD-RG can exploit the spatial local contrast prior to effectively improve the SR performance and the target contrast.

In addition, we visualize the feature maps generate by residual group (RG) and CD-RG with a toy example in Fig. 5. Note that,

the visualization maps are the L2 norm results along the channel dimension [61], [73] and the red and blue boxes represent target areas and edge areas, respectively. As is illustrated in Fig. 5(a), the input frame of the image sequence consists of a target of size  $3 \times 3$  (*i.e.*, the white cube at the top) and the clutter (*i.e.*, the white area at the bottom). It can be observed from Fig. 5(b) and (c) that the target contrast in the feature map extracted by CD-RG is higher than that of RG. This demonstrates that CD-RG can enhance the target contrast (from 7.41 to 13.55). In addition, CD-RG can also improve the contrast between high-frequency edges and background (from 6.64 to 13.59). This is because, CD-RG aggregates the gradient-level information to concentrate more on the high-frequency edge information, thus improving the SR performance and target contrast simultaneously.

Moreover, we conduct ablation experiments to replace all the CD-convs in MoCoPnet by DLCMs. Note that, the training process of the MoCoPnet with DLCMs is unstable with sudden loss divergence due to gradient fracture. By contrast, CD-conv reserves the image feature information to update all pixels, which ensures the gradient propagation continuity. The ablation results in Table I show that CD-conv introduces significant performance gain on PSNR/SSIM (*i.e.*, 1.01/0.039 on average) and further improve the contrast of small targets (*i.e.*, 0.024/0.022 SNR/CR gain on average).

2) *LSTA Module*: In MoCoPnet, two cascaded LSTAs with parameters LSTA (kern=3, dila=3) and LSTA (kern=3, dila=1) are used to enhance the spatio-temporal local features of sequence images in a coarse-to-fine manner. To validate the effectiveness of our design choice, we first remove LSTAs in the MoCoPnet and name the model as LSTA<sub>1</sub>. In addition, we further conduct ablation experiments to investigate the influences of the parameters, numbers, subpixel information exploitation and arrangements of LSTAs on the SR performance. Specifically, we first replace LSTAs in the MoCoPnet by two cascaded LSTAs with parameters (kern=3, dila=1) and name the model as LSTA<sub>2</sub>. Second, we replace LSTAs in the MoCoPnet by an LSTA with parameter (kern=3, dila=1) and name the model as LSTA<sub>3</sub>. Third, we replace LSTAs in the MoCoPnet by an LSTA with parameter (kern=9, dila=1/4) and name the model as LSTA<sub>4</sub>. Fourth, we replace LSTAs in the MoCoPnet by three parallel LSTAs with parameters (kern=3, dila=1), (kern=3, dila=3), (kern=3, dila=5) and name the model as LSTA<sub>5</sub>.

The experimental results of LSTA<sub>1-5</sub> are shown in Table II. It can be observed that the #Params. and FLOPs of LSTA<sub>1-5</sub> are comparable, which means that LSTA only costs a small amount of computations. The PSNR/SSIM/SNR/CR scores of LSTA<sub>1</sub> are 0.28 dB/0.008/0.021/0.013 lower than the MoCoPnet. This demonstrates that LSTA can effectively use the supplementary temporal information to enhance the local features, thus improving the SR performance and the target contrast. The PSNR/SSIM/SNR/CR scores of LSTA<sub>2</sub> are 0.03 dB/0.002/0.003/0.003 lower than the MoCoPnet. This demonstrates that LSTA with larger expansion rate (*i.e.*, dila=3) for coarse processing promotes our network to better extract and utilize temporal information. The PSNR/SSIM/SNR/CR scores of LSTA<sub>3</sub> are 0.16 dB/0.004/0.009/0.006 lower than the MoCoPnet and 0.13 dB/0.003/0.006/0.003 lower than LSTA<sub>2</sub>. This

demonstrates that coarse-to-fine processing benefits SR performance and target enhancement. The PSNR/SSIM/SNR/CR scores of LSTA<sub>4</sub> are slightly higher than LSTA<sub>3</sub> for 0.07 dB/0.001/0.003/0.000 but the memory cost of LSTA<sub>4</sub> is 2 times than LSTA<sub>3</sub> (*i.e.*, 2.46 versus 1.17). This demonstrates subpixel information exploitation benefits the performance of SR and target enhancement but significantly increases the memory cost. The PSNR/SSIM/SNR/CR scores of LSTA<sub>5</sub> are 0.07 dB/0.002/0.005/0.005 lower than the MoCoPnet and 0.09 dB/0.003/0.004/0.001 higher than LSTA<sub>3</sub>. This demonstrates that the cascade mode of LSTAs can better exploit interframe information correlation and SR performance and target enhancement can be further improved by enlarging the receptive field of LSTAs.

Note that, we visualize the feature maps and attention maps generated by LSTA<sub>3</sub> (*i.e.*, an LSTA with kernel size of 3 and dilation rate of 1) with a toy example in Fig. 6. Note that, the visualized feature maps are the L2 norm results along the channel dimension [61], [73]. As is illustrated in Fig. 6(a1), the target with size  $1 \times 1$  (*i.e.*, the white cube) is in the middle of the red reference frame. In Fig. 6(a2), the target is in the top left of the blue neighborhood frame. The corresponding features before LSTA are shown in Fig. 6(b1) and (b2). The aligned feature after LSTA is shown in Fig. 6(b3). It can be observed that LSTA can effectively perform frame alignment to achieve motion compensation. In addition, the attention maps are shown in Fig. 6(c1)–(c9), and the position of each attention map corresponds to the spatial arrangement in Fig. 3(b). It can be observed that Fig. 6(c1) has the highest intensity (more than 90% are 1) and represents the top-left motion, which demonstrates that LSTA can effectively capture the target motion to perform frame alignment.

Finally, we replace LSTAs in the MoCoPnet by an optical-flow module (OFM) and a deformable alignment module (DAM) to compare our LSTA with the widely used optical flow and deformable alignment techniques. The experimental results are listed in Table II. It can be observed that the PSNR/SSIM/SNR/CR scores of the MoCoPnet with LSTAs are higher than the MoCoPnet with OFM and DAM for 0.11 dB/0.004/0.015/0.009 and 0.06 dB/0.002/0.005/0.006, respectively. By contrast, the number of parameters and FLOPs of the MoCoPnet with LSTA modules are lower than the MoCoPnet with OFM and DAM for 0.11 M/2.70 G and 0.19 M/3.80 G, respectively. This demonstrates that LSTA is superior in exploiting the information among frames to improve the SR performance and the target contrast with lower computational cost. This is because, on the one hand, LSTA can directly learn motion compensation by attention mechanism without optical flow estimation and warping, which results in ambiguous and duplicate results [36], [77]. On the other hand, compared with DAM, LSTA can better incorporate the local prior to achieve improved SR performance and the training process of LSTA is more stable to converge to a good result.

In addition, we visualize the feature maps generated by OFM, DAM, and LSTAs with a toy example in Fig. 7. Note that, the visualization maps are the L2 norm results along the channel dimension. As is illustrated in Fig. 7(a), the input image sequence

TABLE II  
ABLATION RESULTS OF THE LSTA MODULE ON THE AVERAGE OF SAITD, HUI,  
AND ANTI-UAV DATASETS

Variants	#Params.	FLOPs	PSNR	SSIM	SNR	CR
LSTA <sub>1</sub>	<b>4.83M</b>	<b>52.60G</b>	30.77	0.851	0.813	12.044
LSTA <sub>2</sub>	<b>4.83M</b>	52.65G	31.02	0.857	0.831	12.054
LSTA <sub>3</sub>	<b>4.83M</b>	52.62G	30.89	0.854	0.825	12.051
LSTA <sub>4</sub>	<b>4.83M</b>	52.62G	30.96	0.855	0.828	12.051
LSTA <sub>5</sub>	4.84M	52.98G	30.98	0.857	0.829	12.052
OFM	4.94M	55.35G	30.94	0.855	0.819	12.048
DAM	5.02M	56.45G	30.99	0.857	0.829	12.051
MoCoPnet	<b>4.83M</b>	52.65G	<b>31.05</b>	<b>0.859</b>	<b>0.834</b>	<b>12.057</b>

Note that, LSTA1 validates the effectiveness of the module and LSTA2-5 investigate the impact of its parameters, numbers, subpixel information exploitation, and arrangements on the SR performance. OFM and DAM validate the superiority of LSTA than the optical flow technique and deformable alignment technique. “#Params.” represents the number of parameters. FLOPs is computed based on HR frames with a resolution of  $256 \times 256$ . Best results are shown in boldface.

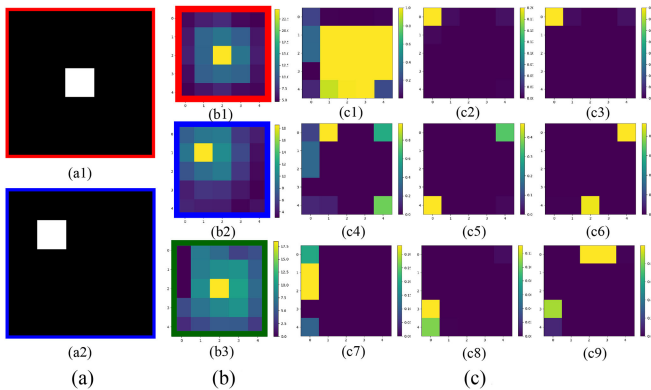


Fig. 6. Toy example illustration of feature maps and attention maps generated by LSTA<sub>3</sub>. (a1) and (a2) Reference frame and neighborhood frame. (b1) and (b2) Reference feature and neighborhood feature before LSTA. (b3) Aligned feature after LSTA. (c1)–(c9) Attention maps of LSTA and the positions correspond to the spatial arrangement in Fig. 3(b). (a) Images. (b) Features. (c) Attention maps.

consists of a random consistent movement of a target with size  $3 \times 3$  (*i.e.*, the white cube) in the background (*i.e.*, the black area). The feature maps before OFM, DAM, and LSTAs are shown in Fig. 7(b), (d), and (f). It can be observed that the target positions in the extracted feature maps are close to the blue dots (*i.e.*, the groundtruth position of the target in the current feature). Then, OFM, DAM, and LSTAs perform feature alignment on the extracted features. As is illustrated in Fig. 7(c), the target positions in the feature maps generated by OFM are close to the blue dots. In Fig. 7(e), the blue dots and the red dots (*i.e.*, the groundtruth position of the target in the reference feature) are both highlighted, which demonstrates that DAM does not perform frame alignment but highlight all the possible positions. The feature maps generated by LSTA1 (kern=3, dila=3) and LSTA2 (kern=3, dila=1) are shown in Fig. 7(e) and (f). As is illustrated in Fig. 7(f), all the target positions in the feature maps generated by LSTA2 are closer to the red dot than those of OFM. This demonstrates that LSTA is superior in motion compensation. Note that, it can be observed from Fig. 7(e) and (f) that LSTA1 and LSTA2 achieve coarse-to-fine alignment to highlight the aligned target. This demonstrates the effectiveness and superiority of our coarse-to-fine alignment strategy.

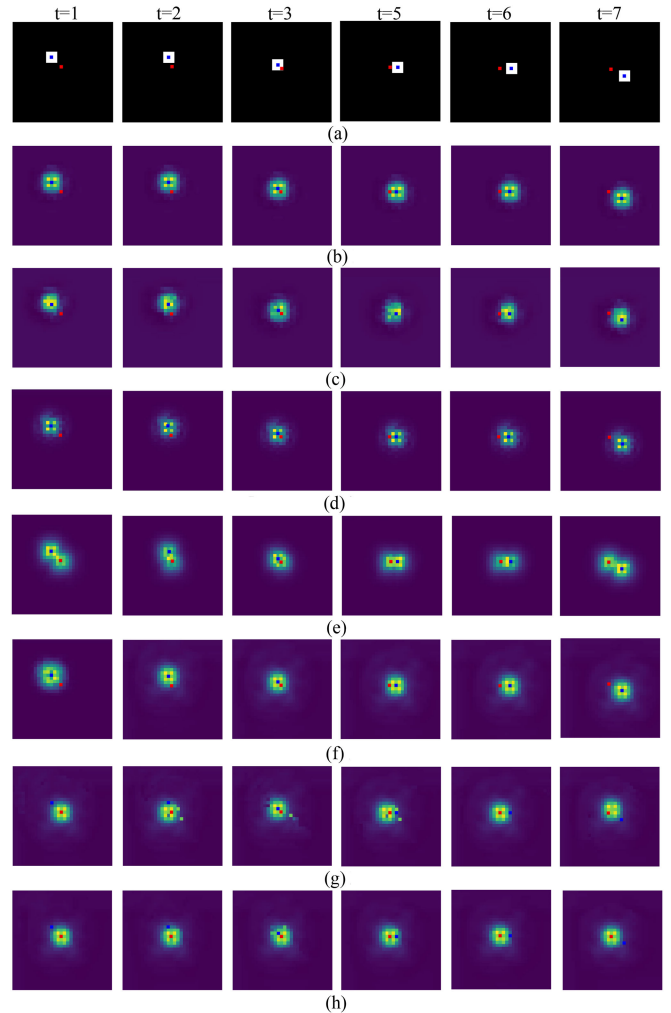


Fig. 7. Toy example illustration of feature maps generated by OFM, DAM, and LSTA. Note that,  $t$  represents the temporal dimension. The blue dot and the red dot represent the groundtruth position of the target in the current feature ( $t \in [1, 3] \cup [5, 7]$ ) and in the reference feature ( $t = 4$ ). (a) Input image sequence. (b) Feature maps before OFM. (c) Feature maps after OFM. (d) Feature maps before DAM. (e) Feature maps after DAM. (f) Feature maps before LSTA. (g) Feature maps after LSTA1. (h) Feature maps after LSTA2.

### C. Comparative Evaluation

In this subsection, we compare our MoCoPnet with one top-performing single image SR methods RCAN [15], five video SR methods VSRnet [74], VESPCN [34], SOF-VSR [35], TDAN [39], and D3Dnet [30], and three infrared image SR methods IERN [51], PSRGAN [52], and ChaSNet [53]. For fair comparison, we retrain all the compared methods on infrared small target dataset [69] and exclude the first and the last two frames of the video sequences for performance evaluation.

1) *SR on Synthetic Images*: PSNR/SSIM results calculated on the whole image are listed in Table III. SNR and CR scores calculated in the local background neighborhood are listed in the 2nd – 9th columns of Table IV. It can be observed that the MoCoPnet achieves the highest scores of PSNR, SSIM, and outperforms most of the compared algorithms on SNR and CR scores. The aforementioned scores demonstrate that our network can effectively recover accurate details and improve



TABLE III  
PSNR/SSIM RESULTS AND RUNNING TIME OF DIFFERENT METHODS ACHIEVED BY SAITD [70], HUI [69], AND ANTI-UAV [71] DATASETS

Methods	VSRnet [74]	VESPCN [34]	RCAN [15]	SOF-VSR [35]	TDAN [39]	D3Dnet [30]	IERN [51]	PSRGAN [52]	ChaSNet [53]	MoCoPnet
SAITD	26.03/0.706	26.57/0.735	26.58/0.735	26.97/0.753	26.11/0.709	27.81/0.794	26.53/0.730	26.49/0.722	26.71/0.760	<b>28.17/0.807</b>
Hui	32.03/0.828	32.33/0.835	32.44/0.836	32.55/0.841	32.17/0.830	32.84/0.850	32.67/0.838	32.36/0.828	32.41/0.824	<b>33.12/0.857</b>
Anti-UAV	31.42/0.904	31.63/0.910	31.73/0.912	31.68/0.912	31.58/0.905	31.81/0.911	31.54/0.909	30.96/0.884	31.73/0.910	<b>31.85/0.914</b>
Average	29.83/0.813	30.18/0.827	30.25/0.828	30.40/0.835	29.95/0.815	30.82/0.852	30.25/0.826	29.94/0.811	30.28/0.831	<b>31.05/0.859</b>
Time (s)	<b>0.157</b>	0.627	11.174	3.788	5.923	7.042	6.578	0.823	13.073	10.343

Note that, the running time is the total time tested on 100 consecutive frames with a input resolution of  $64 \times 64$ . Best results are shown in boldface.

TABLE IV  
SNR AND CR RESULTS OF DIFFERENT METHODS ACHIEVED ON SUPERRESOLVED LR IMAGES (COLUMNS 2ND – 9TH) AND SUPERRESOLVED HR IMAGES (COLUMNS 10TH – 17TH)

Resolution	640×512		256×256		640×640		-		2560×2048		2048×2048		2560×2048		-	
	SAITD		Hui		Anti-UAV		Average		SAITD		Hui		Anti-UAV		Average	
	SNR	CR	SNR	CR	SNR	CR	SNR	CR	SNR	CR	SNR	CR	SNR	CR	SNR	CR
LR	0.666	14.066	0.781	13.583	0.915	6.174	0.787	11.274	-	-	0.986	-	-	-	-	-
Bicubic	<u>0.676</u>	13.780	0.750	15.100	0.817	<b>6.747</b>	0.747	11.875	0.808	<b>14.736</b>	-	<b>15.817</b>	0.958	7.173	0.917	<b>12.575</b>
VSRnet [74]	0.659	14.125	0.776	15.100	0.882	6.726	0.773	11.984	0.672	14.704	1.002	15.661	0.954	<u>7.178</u>	0.876	12.514
VESPCN [34]	0.656	14.118	0.793	15.145	0.920	6.641	0.790	11.968	0.901	14.664	<u>1.005</u>	15.616	0.963	7.115	0.956	12.465
RCAN [15]	0.670	14.213	0.813	15.202	0.952	6.713	0.811	12.043	<u>0.914</u>	14.720	0.997	15.649	0.947	7.168	0.953	12.512
SOF-VSR [35]	0.662	14.175	0.808	15.113	0.932	6.698	0.800	11.995	0.913	14.700	0.997	15.603	<u>0.965</u>	7.168	0.958	12.490
TDAN [39]	0.655	14.206	0.772	15.192	0.882	6.711	0.770	12.036	0.889	14.725	0.999	15.693	0.963	7.173	0.950	12.530
D3Dnet [30]	0.672	<u>14.240</u>	0.845	<b>15.215</b>	<b>0.972</b>	<u>6.736</u>	<u>0.830</u>	<b>12.064</b>	0.907	<u>14.731</u>	<u>1.005</u>	<u>15.699</u>	0.964	7.166	0.959	<u>12.532</u>
IERN [51]	0.665	13.582	0.833	15.155	0.888	6.537	0.795	11.758	0.887	14.320	0.934	15.683	0.960	7.162	0.927	12.389
PSRGAN [52]	<b>0.678</b>	13.767	<u>0.852</u>	14.939	0.941	6.326	0.824	11.677	0.879	14.637	0.942	15.604	0.955	7.158	0.925	12.466
ChaSNet [53]	0.668	13.491	0.793	14.605	0.885	6.050	0.782	11.382	0.899	14.616	0.937	15.623	0.959	7.161	0.932	12.466
MoCoPnet	<b>0.678</b>	<b>14.259</b>	<b>0.859</b>	<u>15.203</u>	<u>0.965</u>	6.709	<b>0.834</b>	<u>12.057</u>	<b>0.922</b>	14.729	<b>1.006</b>	15.685	<b>0.966</b>	<b>7.181</b>	<b>0.965</b>	<u>12.532</u>
HR	0.810	14.262	1.001	15.265	0.959	6.706	0.923	12.078	-	-	-	-	-	-	-	-

Note that, we add the results of LR and HR as the baseline results and the resolution of LR is four times lower than the listed resolution. Exclude LR and HR, best results are shown in boldface and second best results are shown in underlined.

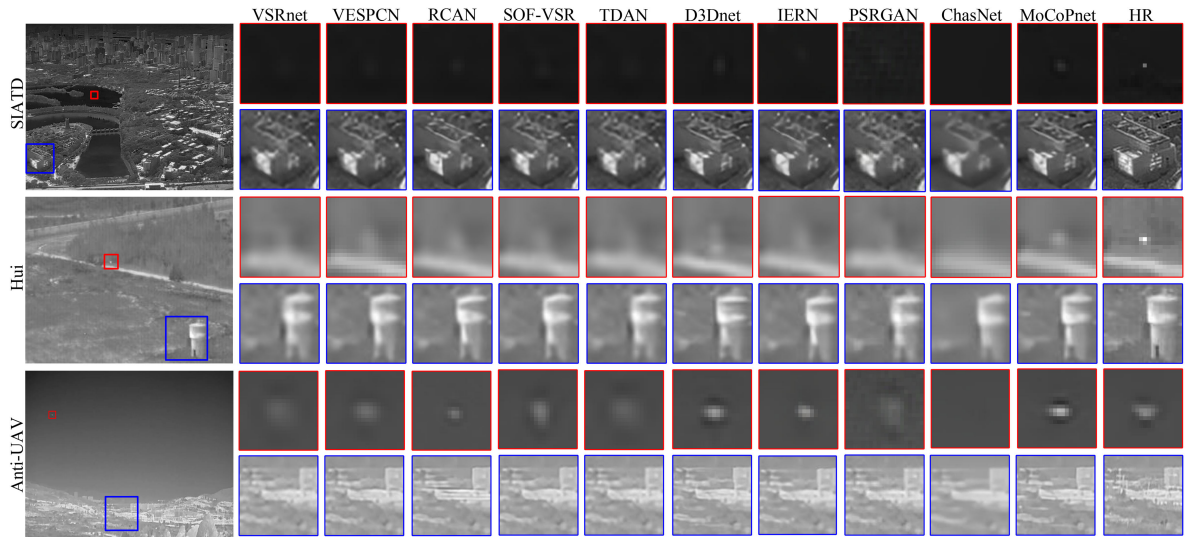


Fig. 8. Visual results of different SR methods on LR images for  $4 \times$  SR.

the target contrast. That is because, LSTA performs implicit motion compensation and CD-RG incorporates the center-orient gradient information to effectively improve the SR performance and the target contrast. Note that, we also analyze the running time of different methods and the results are shown in Table III. The running time is the total time tested on 100 consecutive HR frames with a resolution of  $256 \times 256$  and is averaged over 20 runs. It can be observed that our MoCoPnet

achieves a better SR performance with a reasonable increase in running time.

Qualitative results are shown in Fig. 8. For the SR performance, it can be observed from the blue zoom in regions that the MoCoPnet can recover more accurate details (e.g., the sharp edges of buildings, and the lighthouse details closer to groundtruth HR image). For target enhancement, it can be observed from the red zoom in regions that, in the first row,

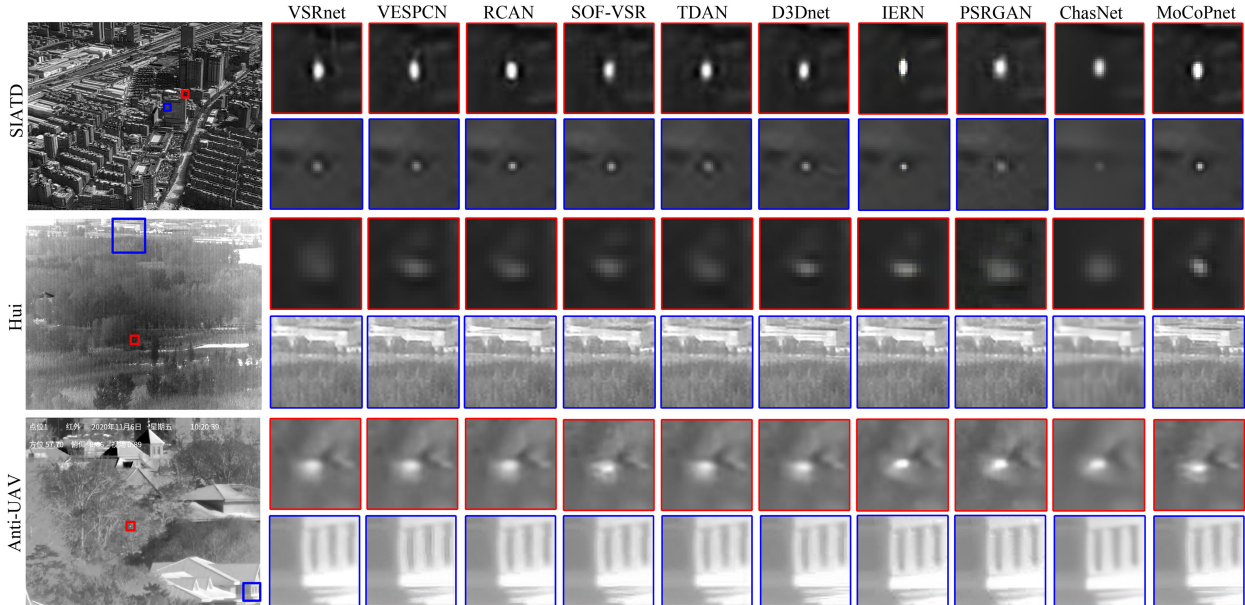


Fig. 9. Visual results of realSR on HR images for  $4\times$  SR.

the MoCoPnet can further improve the target contrast, which is almost invisible in other compared methods. In the second row, the MoCoPnet is more robust to large motion caused by turntable collections [69] (*e.g.*, artifacts in the zoom-in region of D3Dnet). In the third row, the MoCoPnet can effectively improve the target contrast to be even higher than HR images (*i.e.*, 1.82 versus 1.75).

2) *SR on Real Images*: SNR and CR scores calculated in the local background neighborhood of superresolved HR images are listed in the 10th – 17th columns of Table IV. It can be observed that the MoCoPnet can achieve the best SNR score and the second best CR score on the average of test datasets under real-world degradation. This demonstrates the superiority of our method in improving the contrast between targets and background.

Qualitative results are shown in Fig. 9. It can be observed that the MoCoPnet can recover finer details and achieve a better visual quality, such as the edges of building and window. In addition, the MoCoPnet can further improve the intensity and the contour details of the targets.

#### D. Effect on Infrared Small Target Detection Algorithm

In this subsection, we select three typical infrared small target detection algorithms (Top-hat [75], ILCM [76], and IPI [58]) to perform detection on superresolved infrared images. The parameters of the three infrared small target detection algorithms are shown in Table V. When  $4\times$  SR is performed on HR images, the size of filters, block, and stride, as well as the true detection threshold  $\tau$  are enlarged by four times, respectively. When  $4\times$  downsampling is performed on HR images, the filter sizes of Top-hat and ILCM are set to  $3\times 3$ . The block sizes and the stride of IPI are set to  $15\times 15$  and 3. The true detection threshold  $\tau$  is set to 3.0. For simplicity, we only use the best two superresolved results of D3Dnet and MoCoPnet to perform detection. We also

TABLE V  
PARAMETER SETTINGS OF TOP-HAT [75], ILCM [76], AND IPI [58] IN HR IMAGES

Method	Parameters
Top-hat	$5\times 5$ square filter
ILCM	$5\times 5$ filter
IPI	$B=50\times 50, S=10, \lambda = \frac{L}{\sqrt{\min(n_1, n_2, n_3)}}, L=1, \epsilon=10^{-7}$

“B” represents block size and “S” represents stride.

introduce bicubically upsampled (Bicubic) images and HR images as the baseline results.

1) *Detection on Synthetic Images*: The quantitative detection results of superresolved LR images are listed in Table VI. It can be observed that the SNRG, SCRG, and CG of the superresolved images are generally higher than the Bicubic images. This demonstrates that SR algorithms can effectively improve the contrast between the target and the background, thus promoting the detection performance. It is worth noting that the SNRG, SCRG, and CG scores of D3Dnet and MoCoPnet can even surpass those of HR. This is because, SR algorithms can perform better on the high-frequency small targets than the low-frequency local background, thus achieving an improved target contrast than HR images. In addition, Bicubic can achieve the highest BSF score in most cases. This is because SR algorithms act on the entire image, which enhances targets and background simultaneously and detection algorithms have better filtering performance in smoothly changing background. Note that, BSF of the MoCoPnet is generally higher than that of D3Dnet. This is because the MoCoPnet can focus on recovering the local salient features in the image and further improve the contrast between targets and background, which benefits the detection performance.

TABLE VI  
 QUANTITATIVE DETECTION RESULTS OF TOPHAT, ILCM, AND IPI ACHIEVED ON SUPERRESOLVED LR IMAGES IN INFRARED SMALL TARGET DATASETS

Resolution		640×512				256×256				640×640				-			
Methods		SAITD				Hui				Anti-UAV				Average			
		SNRG	BSF	SCRG	CG	SNRG	BSF	SCRG	CG	SNRG	BSF	SCRG	CG	SNRG	BSF	SCRG	CG
Top-hat	Bicubic	0.50	2.55	6.43	<u>3.60</u>	0.93	1.79	15.94	9.66	3.77	4.32	15.58	3.12	1.73	2.89	12.65	5.46
	D3Dnet	0.77	<u>3.10</u>	<b>9.31</b>	<b>4.28</b>	1.49	<b>2.01</b>	<b>20.47</b>	<b>11.20</b>	<u>9.60</u>	6.70	<u>31.05</u>	<b>3.33</b>	<u>3.95</u>	3.94	<b>20.28</b>	<b>6.27</b>
	MoCoPnet	<u>0.82</u>	<b>3.25</b>	<u>9.04</u>	3.55	<u>1.53</u>	<u>1.98</u>	<u>18.88</u>	<u>10.22</u>	<b>13.06</b>	<u>6.72</u>	28.35	2.82	<b>5.14</b>	<u>3.99</u>	<u>18.76</u>	<u>5.53</u>
	HR	<b>1.62</b>	1.84	5.40	3.22	<b>1.73</b>	1.55	8.82	5.30	7.61	<b>13.18</b>	<b>74.73</b>	<u>2.99</u>	3.65	<b>5.52</b>	29.65	3.83
ILCM	Bicubic	1.07	<b>1.20</b>	5.93	4.89	0.96	<b>0.91</b>	3.73	4.34	0.90	<b>0.83</b>	1.82	2.15	0.97	<b>0.98</b>	3.83	3.79
	D3Dnet	1.07	<u>1.02</u>	7.29	7.15	1.08	<u>0.84</u>	8.01	10.03	<b>1.07</b>	<u>0.77</u>	2.84	3.72	1.07	<u>0.87</u>	6.05	6.96
	MoCoPnet	<u>1.08</u>	1.00	<u>7.91</u>	<u>7.91</u>	<u>1.09</u>	<u>0.84</u>	<u>8.21</u>	<u>10.12</u>	<b>1.07</b>	0.76	<b>3.30</b>	<u>4.47</u>	1.08	<u>0.87</u>	<u>6.47</u>	<u>7.50</u>
	HR	<b>1.37</b>	0.89	<b>11.85</b>	<b>13.20</b>	<b>1.31</b>	0.77	<b>10.88</b>	<b>15.39</b>	<u>1.05</u>	0.70	<u>3.14</u>	<b>4.54</b>	<b>1.24</b>	0.79	<b>8.62</b>	<b>11.04</b>
IPI	Bicubic	5.1e7	<b>2.1e10</b>	1.6e7	1e-3	6.2e9	<b>1.1e10</b>	2.1e9	0.82	9.8e9	<b>9.9e9</b>	3.3e9	0.06	5.3e9	<b>1.4e10</b>	1.8e9	0.29
	D3Dnet	1.9e8	<u>4.0e9</u>	2.1e8	0.07	<u>1.9e10</u>	<u>5.0e9</u>	<u>3.5e9</u>	0.96	<u>2.0e10</u>	3.2e9	<u>4.1e9</u>	<u>0.13</u>	<u>1.3e10</u>	4.1e9	<u>2.6e9</u>	<u>0.39</u>
	MoCoPnet	<u>3.5e8</u>	2.7e9	<u>6.4e8</u>	<u>0.11</u>	<b>2.0e10</b>	4.5e9	<b>4.6e9</b>	<b>1.12</b>	<b>4.2e10</b>	<u>5.4e9</u>	<b>8.1e9</b>	<u>0.13</u>	<b>2.1e10</b>	<u>4.2e9</u>	<b>4.4e9</b>	<b>0.45</b>
	HR	<b>1.1e10</b>	2.6e9	<b>2.3e9</b>	<b>0.13</b>	0.60	2.2e9	8.63	0.61	8.0e9	1.5e9	1.3e9	<b>0.16</b>	6.2e9	2.1e9	1.2e9	0.30

Best results are shown in boldface and second best results are shown in underlined.

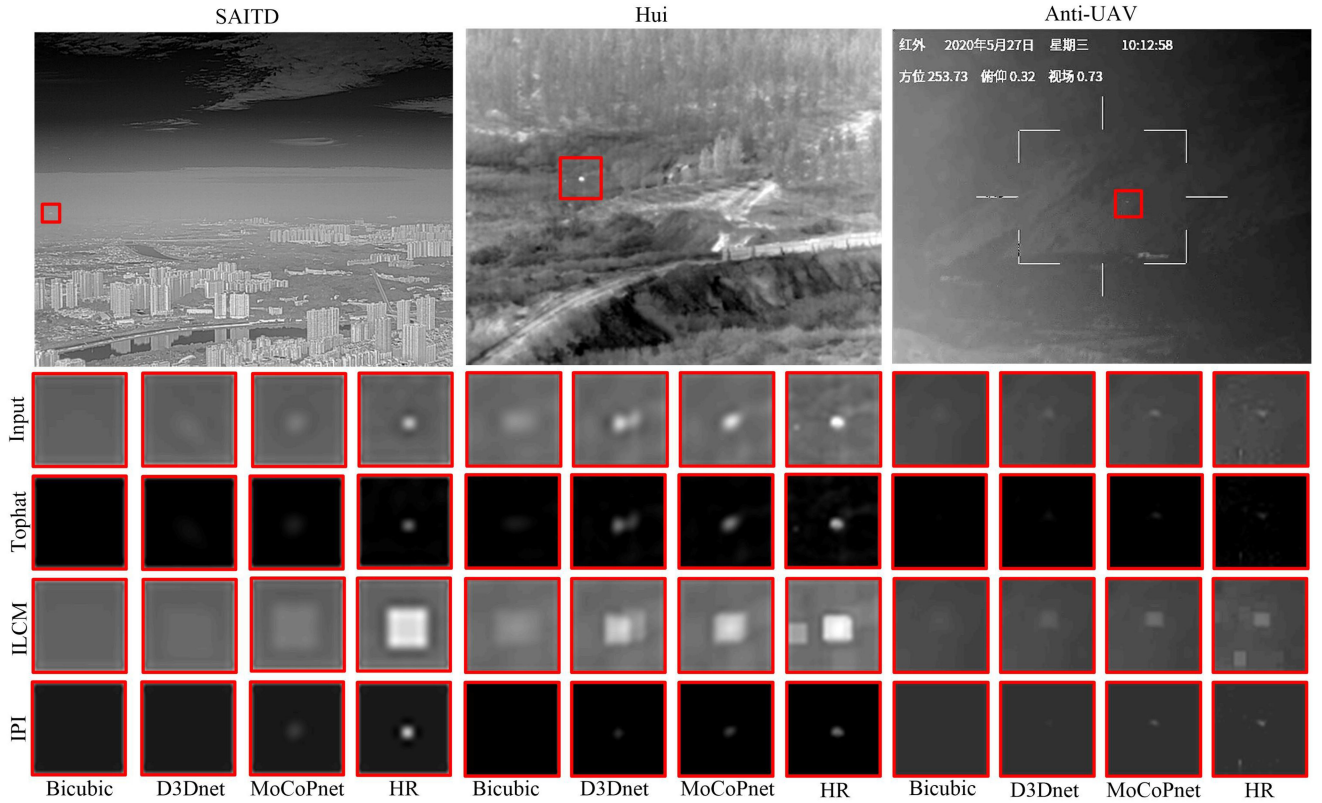


Fig. 10. Qualitative results of superresolved LR image and detection results in SAITD, Hui, and Anti-UAV datasets.

The qualitative results of superresolved LR images and detection results are shown in Fig. 10. In the LR images, the targets intensity are very low (*e.g.*, the targets in SAITD and Anti-UAV are almost invisible). In the superresolved images, the targets intensity are higher and closer to the HR images. This is because, SR algorithms can effectively use the spatio-temporal information to enhance the target contrast. Note that, our MoCoPnet is more robust to large motion caused by turntable collections [69] (*i.e.*, artifacts in the zoom-in region of D3Dnet in Hui dataset). In addition, the neighborhood noise in HR image are suppressed

by the way of downsampling, and then, SR (*e.g.*, point noise are not exist in the zoom-in regions of Hui and Anti-UAV datasets). Then, we perform detection on the superresolved images. It can be observed in Fig. 10 that all the detection algorithms have a poor performance on the Bicubic images (*e.g.*, the target intensity in the target image is very low and almost invisible in all detection results). This is because, bicubic interpolation cannot introduce additional information. However, the targets intensity in the target images of superresolved images are higher than the Bicubic images. Among the superresolved

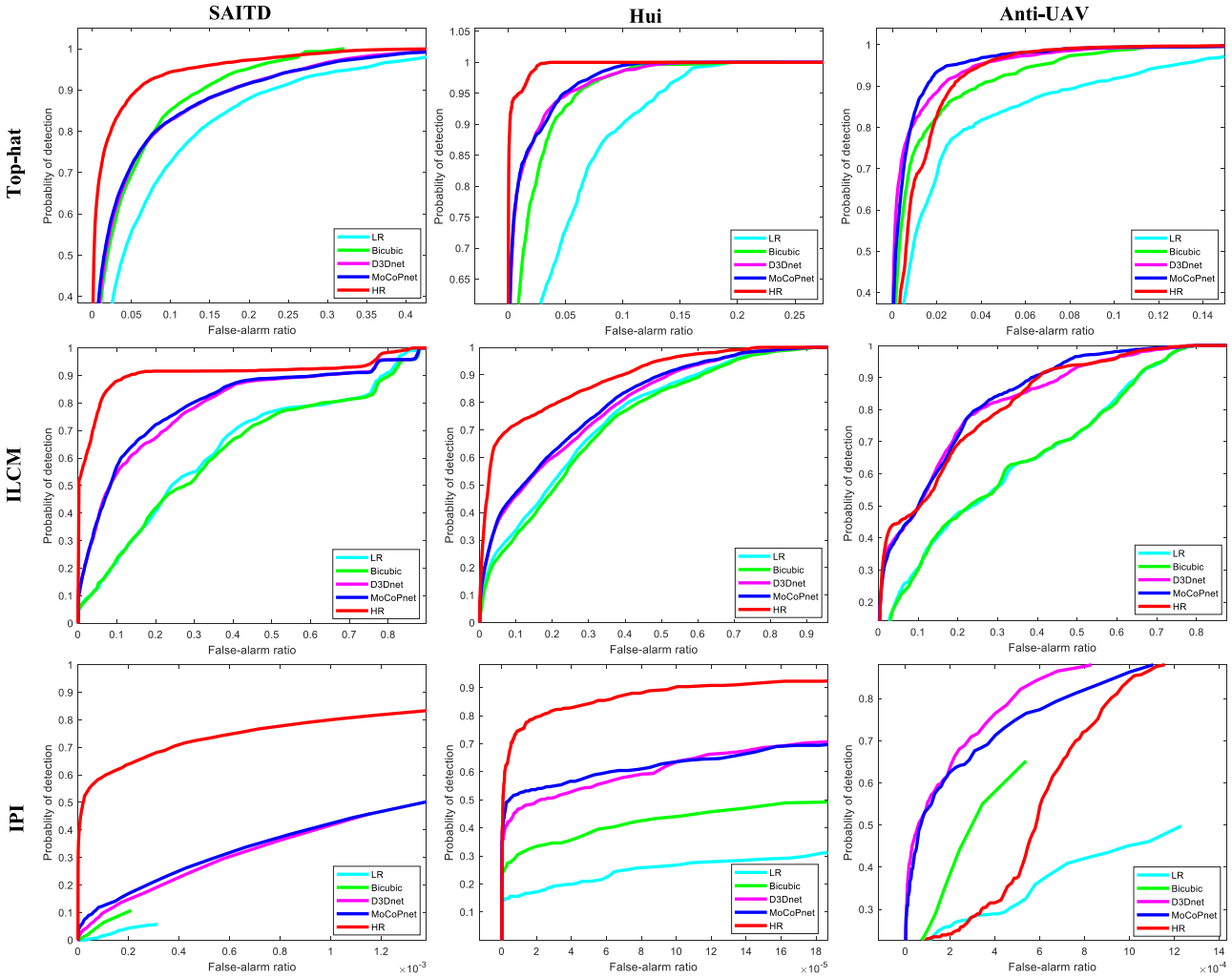


Fig. 11. ROC results of Tophat, ILCM, and IPI achieved on superresolved LR images in SAITD, Hui, and Anti-UAV datasets.

images, the MoCoPnet is superior than D3Dnet in improving the target contrast due to the center-oriented gradient-aware feature extraction of CD-RG and the effective spatio-temporal information exploitation of LSTA.

To evaluate the detection performance comprehensively, we further calculate the ROC results, which are shown in Fig. 11. Note that, ROC results on LR and HR image are used as the baseline results. The targets in HR images have the highest intensity. Therefore, a high detection probability and low false alarm probability can be obtained and the detection probability reaches 1 faster (*e.g.*, the ROC results reach 1 the fast in SAITD and Hui datasets). Downsampling leads to target intensity reduction, thus reducing the detection probability and increasing the false alarms probability. Bicubic introduces no additional image prior information, therefore, LR and Bicubic have the worst detection performance and the ROC results are significant lower than other algorithms (*e.g.*, the ROC results of LR are the lowest and those of Bicubic are the second lowest except the ROC of Tophat in the SAITD dataset). SR algorithms can introduce prior information to improve the contrast between targets and background, thus achieving an improved detection

accuracy (*e.g.*, the ROC results of MoCoPnet and D3Dnet are higher than Bicubic in SAITD and Hui datasets and even higher than HR in Anti-UAV dataset). Note that, false alarm rates of LR and Bicubic can only reach a relatively low value. This is because, IPI achieves detection by sparse and low rank recovery, which significantly decreases the false alarm rate than Tophat and ILCM. From another point, IPI suffers a low detection rate of low contrast targets. Therefore, the ROC curves of Bicubic and LR images are shorter than those of HR and superresolved images. The aforementioned experimental results show that SR algorithms can recover high-contrast targets, thus improving the detection performance.

2) *Detection on Real Images:* The quantitative detection results of superresolved HR images are listed in Table VII. It can be observed that the detection performance of SR algorithms is superior to Bicubic. This demonstrates that the MoCoPnet and D3Dnet can effectively improve the contrast between targets and background, resulting in performance gain of detection. Among SR algorithms, due to the superior performance of SR and target enhancement by our well-designed modules, the MoCoPnet can achieve the best SNRG, SCRG, and CG scores

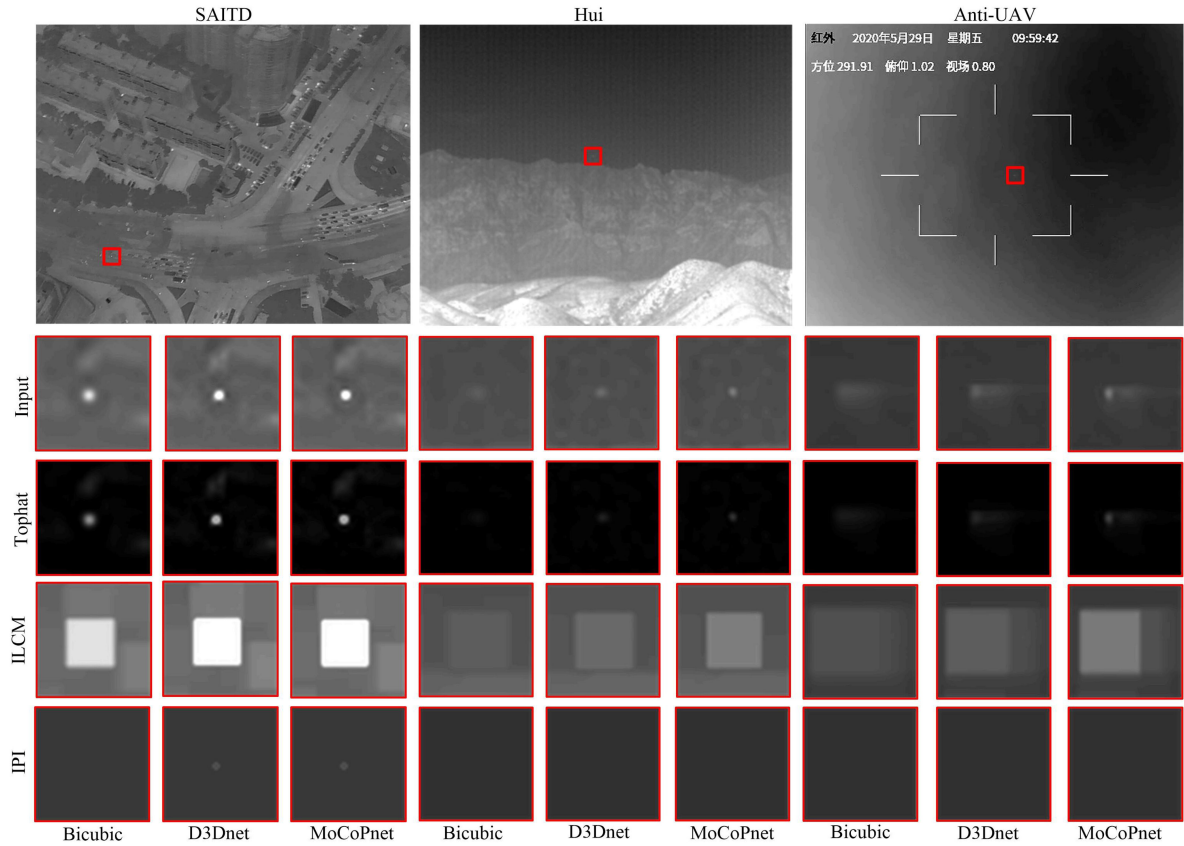


Fig. 12. Qualitative results of superresolved HR image and detection results in SAITD, Hui, and Anti-UAV datasets.

TABLE VII  
QUANTITATIVE DETECTION RESULTS OF TOPHAT, ILCM, AND IPI ACHIEVED ON SUPERRESOLVED HR IMAGES IN INFRARED SMALL TARGET DATASETS

Resolution		2560×2048				2048×2048				2560×2560				-			
Methods		SAITD				Hui				Anti-UAV				Average			
		SNRG	BSF	SCRG	CG	SNRG	BSF	SCRG	CG	SNRG	BSF	SCRG	CG	SNRG	BSF	SCRG	CG
Top-hat	Bicubic	1.01	<b>1.79</b>	4.45	2.78	1.19	<b>1.82</b>	<b>6.09</b>	<u>3.03</u>	<b>4.66</b>	6.95	49.83	<i>4.40</i>	<b>2.28</b>	<u>3.52</u>	20.13	3.40
	D3Dnet	<u>1.27</u>	<u>1.70</u>	<b>4.67</b>	<b>2.95</b>	<b>1.21</b>	1.74	5.63	2.98	<u>3.21</u>	<b>7.39</b>	<b>59.37</b>	<u>4.40</u>	1.90	<b>3.61</b>	<b>23.22</b>	<u>3.44</u>
	MoCoPnet	<b>1.33</b>	<u>1.70</u>	<u>4.60</u>	<u>2.87</u>	<u>1.20</u>	<u>1.78</u>	<u>5.88</u>	<b>3.11</b>	3.20	<u>7.35</u>	<u>58.17</u>	<b>4.53</b>	<u>1.91</u>	<b>3.61</b>	<u>22.88</u>	<b>3.50</b>
ILCM	Bicubic	1.20	<b>0.90</b>	9.02	11.10	<u>0.97</u>	<b>0.84</b>	9.72	11.76	<u>1.00</u>	<b>0.86</b>	7.77	8.71	1.06	<b>0.86</b>	8.84	10.52
	D3Dnet	<u>1.37</u>	<u>0.85</u>	<u>12.65</u>	<u>16.53</u>	<b>1.04</b>	<u>0.78</u>	<b>10.54</b>	<u>13.94</u>	<b>1.02</b>	<u>0.85</u>	<u>8.58</u>	<u>9.60</u>	<u>1.14</u>	<u>0.82</u>	<u>10.59</u>	<u>13.35</u>
	MoCoPnet	<b>1.40</b>	<u>0.85</u>	<b>12.86</b>	<b>16.90</b>	<b>1.04</b>	0.76	<u>10.50</u>	<b>14.18</b>	<b>1.02</b>	<u>0.85</u>	<b>8.71</b>	<b>9.75</b>	<b>1.15</b>	<u>0.82</u>	<b>10.69</b>	<b>13.61</b>
IPI	Bicubic	2.5e9	<b>3.9e9</b>	2.8e8	0.039	<b>5.1e10</b>	<b>2.6e10</b>	1.3e10	0.14	<b>1.7e9</b>	<b>1.2e9</b>	<b>3.0e8</b>	0.046	<b>1.8e10</b>	<b>1.0e10</b>	4.6e9	0.074
	D3Dnet	<u>3.4e9</u>	<u>2.9e9</u>	<u>3.1e8</u>	<b>0.048</b>	<u>4.8e10</u>	<u>1.9e10</u>	<u>1.6e10</u>	<u>0.16</u>	<u>3.5e8</u>	<u>4.0e7</u>	<u>7.9e7</u>	<u>0.048</u>	<u>1.7e10</u>	<u>7.2e9</u>	<u>5.4e9</u>	<u>0.086</u>
	MoCoPnet	<b>3.6e9</b>	2.6e9	<b>3.2e8</b>	<u>0.044</u>	3.7e10	1.6e10	<b>1.7e10</b>	<b>0.18</b>	0.23	20.90	9.95	<b>0.049</b>	1.3e10	6.2e9	<b>5.9e9</b>	<b>0.092</b>

Best results are shown in boldface and second best results are shown in underlined.

in most cases. Note that, the SNRG and SCRG scores (achieved by IPI) of the MoCoPnet in anti-UAV dataset are 7–8 orders of magnitude lower than those of Bicubic and D3Dnet. First of all, the MoCoPnet can achieve highest scores of CG. This demonstrates the target intensity can be effectively and further enhanced by the MoCoPnet. Then, the differences come from the performance of background suppression. Since the MoCoPnet can achieve higher scores of the SR performance than Bicubic and D3Dnet, the local backgrounds of Bicubic and D3Dnet are more gentle and detection algorithms can achieve a better suppression performance. IPI is superior in suppressing background clutter, therefore, sometimes the local backgrounds in the target

image of Bicubic and D3Dnet are zero. Since we add  $\epsilon$  to each denominator in (6)–(9) to prevent it from being zero, SNRG and SCRG scores can be very large due to completely suppressed background. In addition, bicubic interpolation suppresses the high-frequency components to a certain extent, resulting in an optimal BSF value.

The qualitative results of superresolved HR images and detection results are shown in Fig. 12. It can be observed that the targets of Bicubic images are blur, while SR can enhance the intensity of target (*e.g.*, the highlighted and sharpened targets). After processed by SR algorithms, we then perform detection on the superresolved images. Note that, SR algorithms can

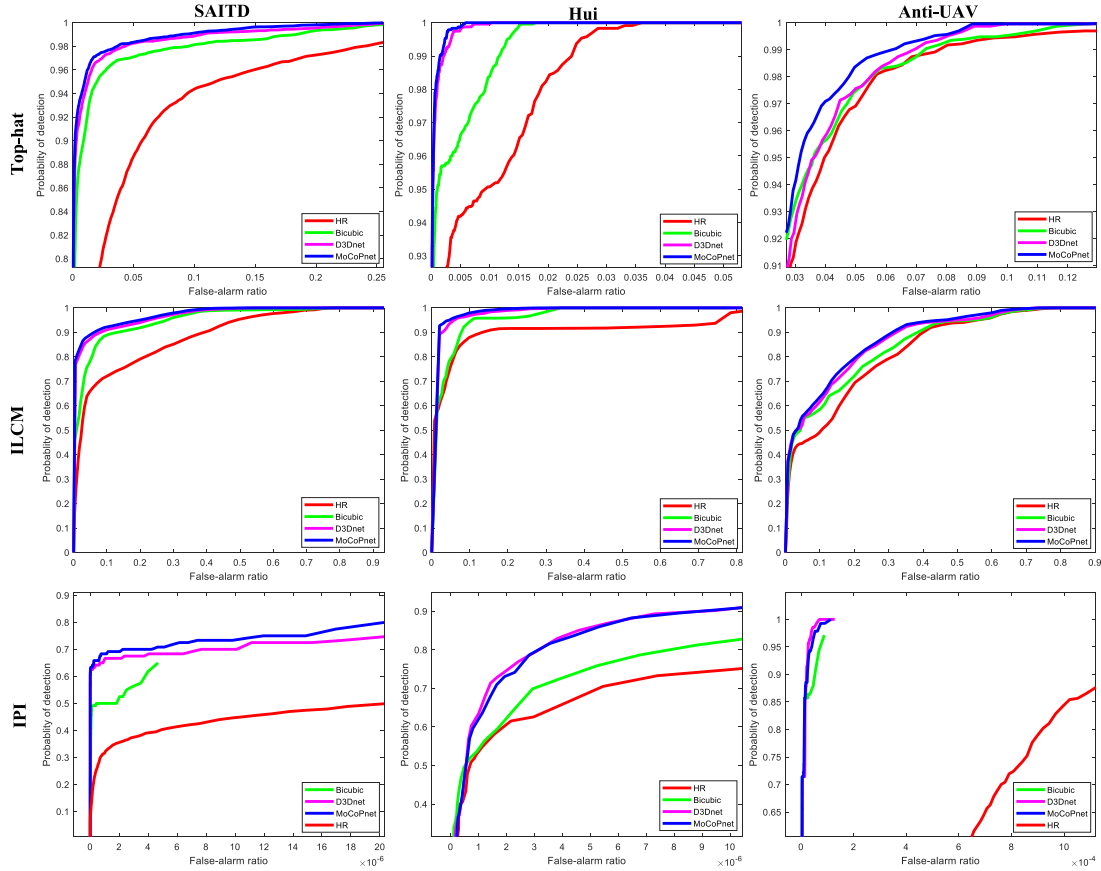


Fig. 13. ROC results of Tophat, ILCM, and IPI achieved on superresolved HR images in SAITD, Hui, and Anti-UAV datasets.

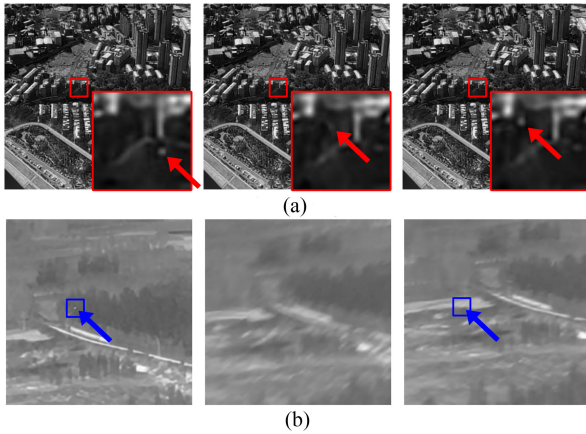


Fig. 14. Failure cases caused by (a) repaid moving targets and (b) sudden changes caused by turnable collection. Red and blue arrows indicate the locations of the targets. (a) Rapid moving target. (b) Sudden change by turnable collection.

effectively improve the intensity of targets and the contrast against background, resulting in a better detection performance.

To evaluate the detection performance comprehensively, we further present the ROC results in Fig. 13. Note that, ROC results on the HR image are used as the baseline results. It can be observed that SR algorithms can improve the detection probability and reduce the false alarm probability in most cases. Compared with D3Dnet, the MoCoPnet can further improve the

target contrast, thus promoting the detection performance. Note that, false alarm rates of Bicubic can only reach a relatively low value. This is because, IPI achieves detection by sparse and low rank recovery, which significantly decreases the false alarm rate than Tophat and ILCM. In other words, IPI suffers low detection rate of low contrast targets.

### E. Limitation

The proposed method fails when the image sequence contains repaid moving targets [see Fig. 14(a)] or sudden changes [see Fig. 14(b)] caused by turnable collections. As we do not have a specific design for handling large motion and sudden change, the motion compensation by LSTAs in these cases can be wrong and our approach may not be able to effectively recover the targets. In future work, we aim to improve the robustness of our method to large motion and sudden change.

## V. CONCLUSION

In this article, we propose a local MoCoPnet for infrared small target SR. Experimental results show that the MoCoPnet can effectively recover the image details and enhance the contrast between targets and background. Based on the superresolved images, we further investigate the effect of SR algorithms on the detection performance. Experimental results show that the MoCoPnet can improve the performance of infrared small target detection.

## REFERENCES

- [1] Y. Dai, Y. Wu, F. Zhou, and K. Barnard, "Asymmetric contextual modulation for infrared small target detection," in *Proc. IEEE Winter Conf. Appl. Comput. Vis.*, 2021, pp. 949–958.
- [2] H.-K. Liu, L. Zhang, and H. Huang, "Small target detection in infrared videos based on spatio-temporal tensor model," *IEEE Trans. Geosci. Remote Sens.*, vol. 58, no. 12, pp. 8689–8700, Dec. 2020.
- [3] Y. Sun, J. Yang, and W. An, "Infrared dim and small target detection via multiple subspace learning and spatial-temporal patch-tensor model," *IEEE Trans. Geosci. Remote Sens.*, vol. 59, no. 5, pp. 3737–3752, May 2021.
- [4] Y. Qin and B. Li, "Effective infrared small target detection utilizing a novel local contrast method," *IEEE Geosci. Remote Sens. Lett.*, vol. 13, no. 12, pp. 1890–1894, Dec. 2016.
- [5] Y. Dai, Y. Wu, F. Zhou, and K. Barnard, "Attentional local contrast networks for infrared small target detection," *IEEE Trans. Geosci. Remote Sens.*, vol. 59, no. 11, pp. 9813–9824, Nov. 2021.
- [6] M. Irani and S. Peleg, "Improving resolution by image registration," *Graphical Models Image Process.*, vol. 53, no. 3, pp. 231–239, 1991.
- [7] R. Keys, "Cubic convolution interpolation for digital image processing," *IEEE Trans. Acoust., Speech, Signal Process.*, vol. 29, no. 6, pp. 1153–1160, Dec. 1981.
- [8] J. Sun, Z. Xu, and H. Shum, "Image super-resolution using gradient profile prior," in *Proc. IEEE Conf. Comput. Vis. Pattern Recognit.*, 2008, pp. 1–8.
- [9] G. Freedman and R. Fattal, "Image and video upscaling from local self-examples," *ACM Trans. Graph.*, vol. 30, no. 2, pp. 1–11, 2011.
- [10] K. Kim and Y. Kwon, "Single-image super-resolution using sparse regression and natural image prior," *IEEE Trans. Pattern Anal. Mach. Intell.*, vol. 32, no. 6, pp. 1127–1133, Jun. 2010.
- [11] Z. Xiong, X. Sun, and F. Wu, "Robust web image/video super-resolution," *IEEE Trans. Image Process.*, vol. 19, no. 8, pp. 2017–2028, Aug. 2010.
- [12] H. Chang, D. Yeung, and Y. Xiong, "Super-resolution through neighbor embedding," in *Proc. IEEE Comput. Soc. Conf. Comput. Vis. Pattern Recognit.*, 2004, vol. 1, pp. 1–I.
- [13] J. Yang, J. Wright, T. Huang, and Y. Ma, "Image super-resolution as sparse representation of raw image patches," in *Proc. IEEE Conf. Comput. Vis. Pattern Recognit.*, 2008, pp. 1–8.
- [14] J. Yang, J. Wright, T. Huang, and Y. Ma, "Image super-resolution via sparse representation," *IEEE Trans. Image Process.*, vol. 19, no. 11, pp. 2861–2873, Nov. 2010.
- [15] Y. Zhang, K. Li, K. Li, L. Wang, B. Zhong, and Y. Fu, "Image super-resolution using very deep residual channel attention networks," in *Proc. Eur. Conf. Comput. Vis.*, 2018, pp. 286–301.
- [16] L. Wang *et al.*, "Parallax attention for unsupervised stereo correspondence learning," *IEEE Trans. Pattern Anal. Mach. Intell.*, vol. 44, no. 4, pp. 2108–2125, Apr. 2022.
- [17] C. Dong, C. Loy, K. He, and X. Tang, "Learning a deep convolutional network for image super-resolution," in *Proc. Eur. Conf. Comput. Vis.*, 2014, pp. 184–199.
- [18] J. Kim, L. Kwon, and L. Mu, "Accurate image super-resolution using very deep convolutional networks," in *Proc. IEEE Conf. Comput. Vis. Pattern Recognit.*, 2016, pp. 1646–1654.
- [19] B. Lim, S. Son, H. Kim, S. Nah, and K. Mu Lee, "Enhanced deep residual networks for single image super-resolution," in *Proc. IEEE Conf. Comput. Vis. Pattern Recognit. Workshops*, 2017, pp. 136–144.
- [20] J. Li, Y. Yuan, K. Mei, and F. Fang, "Lightweight and accurate recursive fractal network for image super-resolution," in *Proc. IEEE/CVF Int. Conf. Comput. Vis. Workshops*, 2019, pp. 3814–3823.
- [21] J. Kim, L. Kwon, and L. Mu, "Deeply-recursive convolutional network for image super-resolution," in *Proc. IEEE Conf. Comput. Vis. Pattern Recognit.*, 2016, pp. 1637–1645.
- [22] Y. Tai, J. Yang, and X. Liu, "Image super-resolution via deep recursive residual network," in *Proc. IEEE Conf. Comput. Vis. Pattern Recognit.*, 2017, pp. 3147–3155.
- [23] K. Jiang, Z. Wang, P. Yi, and J. Jiang, "Hierarchical dense recursive network for image super-resolution," *Pattern Recognit.*, vol. 107, 2020, Art. no. 107475.
- [24] J. Li, F. Fang, J. Li, K. Mei, and G. Zhang, "MDCN: Multi-scale dense cross network for image super-resolution," *IEEE Trans. Circuits Syst. Video Technol.*, vol. 31, no. 7, pp. 2547–2561, Jul. 2020.
- [25] T. Tong, G. Li, X. Liu, and Q. Gao, "Image super-resolution using dense skip connections," in *Proc. IEEE Conf. Comput. Vis. Pattern Recognit.*, 2017, pp. 4799–4807.
- [26] Y. Zhang, Y. Tian, Y. Kong, B. Zhong, and Y. Fu, "Residual dense network for image super-resolution," in *Proc. IEEE Conf. Comput. Vis. Pattern Recognit.*, 2018, pp. 2472–2481.
- [27] T. Dai, J. Cai, Y. Zhang, S.-T. Xia, and L. Zhang, "Second-order attention network for single image super-resolution," in *Proc. IEEE Conf. Comput. Vis. Pattern Recognit.*, 2019, pp. 11065–11074.
- [28] C. Ledig *et al.*, "Photo-realistic single image super-resolution using a generative adversarial network," in *Proc. IEEE Conf. Comput. Vis. Pattern Recognit.*, 2017, pp. 4681–4690.
- [29] X. Wang *et al.*, "ESRGAN: Enhanced super-resolution generative adversarial networks," in *Proc. Eur. Conf. Comput. Vis.*, 2018, pp. 63–79.
- [30] X. Ying, L. Wang, Y. Wang, W. Sheng, W. An, and Y. Guo, "Deformable 3D convolution for video super-resolution," *IEEE Signal Process. Lett.*, vol. 27, pp. 1500–1504, Jul. 2020.
- [31] C. Liu and D. Sun, "On Bayesian adaptive video super resolution," *IEEE Trans. Pattern Anal. Mach. Intell.*, vol. 36, no. 2, pp. 346–360, Feb. 2014.
- [32] M. Ben-Ezra, A. Zomet, and S. K. Nayar, "Video super-resolution using controlled subpixel detector shifts," *IEEE Trans. Pattern Anal. Mach. Intell.*, vol. 27, no. 6, pp. 977–987, Jun. 2005.
- [33] R. Liao, X. Tao, R. Li, Z. Ma, and J. Jia, "Video super-resolution via deep draft-ensemble learning," in *Proc. IEEE Int. Conf. Comput. Vis.*, 2015, pp. 531–539.
- [34] J. Caballero *et al.*, "Real-time video super-resolution with spatio-temporal networks and motion compensation," in *Proc. IEEE Conf. Comput. Vis. Pattern Recognit.*, 2017, pp. 4778–4787.
- [35] L. Wang, Y. Guo, L. Liu, Z. Lin, X. Deng, and W. An, "Deep video super-resolution using HR optical flow estimation," *IEEE Trans. Image Process.*, vol. 29, pp. 4323–4336, Jan. 2020.
- [36] T. Isobe *et al.*, "Video super-resolution with temporal group attention," in *Proc. IEEE Conf. Comput. Vis. Pattern Recognit.*, 2020, pp. 8008–8017.
- [37] J. Dai *et al.*, "Deformable convolutional networks," in *Proc. IEEE Int. Conf. Comput. Vis.*, 2017, pp. 764–773.
- [38] X. Zhu, H. Hu, S. Lin, and J. Dai, "Deformable convnets v2: More deformable, better results," in *Proc. IEEE Conf. Comput. Vis. Pattern Recognit.*, 2019, pp. 9308–9316.
- [39] Y. Tian, Y. Zhang, Y. Fu, and C. Xu, "TDAN: Temporally deformable alignment network for video super-resolution," in *Proc. IEEE/CVF Int. Conf. Comput. Vis. Pattern Recognit.*, 2020, pp. 3357–3366.
- [40] X. Wang, K. C. Chan, K. Yu, C. Dong, and C. Change Loy, "EDVR: Video restoration with enhanced deformable convolutional networks," in *Proc. IEEE/CVF Conf. Comput. Vis. Pattern Recognit. Workshops*, 2019, pp. 1954–1963.
- [41] Y. Jo, S. Wug Oh, J. Kang, and S. Joo Kim, "Deep video super-resolution network using dynamic upsampling filters without explicit motion compensation," in *Proc. IEEE Conf. Comput. Vis. Pattern Recognit.*, 2018, pp. 3224–3232.
- [42] S. Li, F. He, B. Du, L. Zhang, Y. Xu, and D. Tao, "Fast spatio-temporal residual network for video super-resolution," in *Proc. IEEE/CVF Conf. Comput. Vis. Pattern Recognit.*, 2019, pp. 10514–10523.
- [43] Y. Huang, W. Wang, and L. Wang, "Video super-resolution via bidirectional recurrent convolutional networks," *IEEE Trans. Pattern Anal. Mach. Intell.*, vol. 40, no. 4, pp. 1015–1028, Apr. 2018.
- [44] X. Zhu, Z. Li, X. Zhang, C. Li, Y. Liu, and Z. Xue, "Residual invertible spatio-temporal network for video super-resolution," in *Proc. AAAI Conf. Artif. Intell.*, 2019, vol. 33, pp. 5981–5988.
- [45] P. Yi, Z. Wang, K. Jiang, J. Jiang, and J. Ma, "Progressive fusion video super-resolution network via exploiting non-local spatio-temporal correlations," in *Proc. IEEE Int. Conf. Comput. Vis.*, 2019, pp. 3106–3115.
- [46] Y. Mao, Y. Wang, J. Zhou, and H. Jia, "An infrared image super-resolution reconstruction method based on compressive sensing," *Infrared Phys. Technol.*, vol. 76, pp. 735–739, 2016.
- [47] X. Zhang, C. Li, Q. Meng, S. Liu, Y. Zhang, and J. Wang, "Infrared image super resolution by combining compressive sensing and deep learning," *Sensors*, vol. 18, no. 8, 2018, Art. no. 2587.
- [48] T. Y. Han, Y. J. Kim, and B. C. Song, "Convolutional neural network-based infrared image super resolution under low light environment," in *Proc. Eur. Signal Process. Conf.*, 2017, pp. 803–807.
- [49] Z. He, S. Tang, J. Yang, Y. Cao, M. Y. Yang, and Y. Cao, "Cascaded deep networks with multiple receptive fields for infrared image super-resolution," *IEEE Trans. Circuits Syst. Video Technol.*, vol. 29, no. 8, pp. 2310–2322, Aug. 2019.
- [50] Q.-M. Liu, R.-S. Jia, Y.-B. Liu, H.-B. Sun, J.-Z. Yu, and H.-M. Sun, "Infrared image super-resolution reconstruction by using generative adversarial network with an attention mechanism," *Appl. Intell.*, vol. 51, no. 4, pp. 2018–2030, 2021.

- [51] L. Chen, R. Tang, M. Anisetti, and X. Yang, "A lightweight iterative error reconstruction network for infrared image super-resolution in smart grid," *Sustain. Cities Soc.*, vol. 66, 2021, Art. no. 102520.
- [52] Y. Huang, Z. Jiang, R. Lan, S. Zhang, and K. Pi, "Infrared image super-resolution via transfer learning and PSRGAN," *IEEE Signal Process. Lett.*, vol. 28, pp. 982–986, May 2021.
- [53] K. Prajapati *et al.*, "Channel split convolutional neural network (ChaSnet) for thermal image super-resolution," in *Proc. IEEE Conf. Comput. Vis. Pattern Recognit.*, 2021, pp. 4368–4377.
- [54] X. Yang, M. Zhang, W. Li, and R. Tao, "Visible-assisted infrared image super-resolution based on spatial attention residual network," *IEEE Geosci. Remote Sens. Lett.*, vol. 19, pp. 1–5, 2022, Art. no. 7002705.
- [55] J. Hu, L. Shen, and G. Sun, "Squeeze-and-excitation networks," in *Proc. IEEE Conf. Comput. Vis. Pattern Recognit.*, 2018, pp. 7132–7141.
- [56] S. Anwar and N. Barnes, "Real image denoising with feature attention," in *Proc. IEEE Int. Conf. Comput. Vis.*, 2019, pp. 3155–3164.
- [57] L. Wang *et al.*, "Exploring sparsity in image super-resolution for efficient inference," in *Proc. IEEE/CVF Conf. Comput. Vis. Pattern Recognit.*, 2021, pp. 4915–4924.
- [58] C. Gao, D. Meng, Y. Yang, Y. Wang, X. Zhou, and A. G. Hauptmann, "Infrared patch-image model for small target detection in a single image," *IEEE Trans. Image Process.*, vol. 22, no. 12, pp. 4996–5009, Dec. 2013.
- [59] C. P. Chen, H. Li, Y. Wei, T. Xia, and Y. Y. Tang, "A local contrast method for small infrared target detection," *IEEE Trans. Geosci. Remote Sens.*, vol. 52, no. 1, pp. 574–581, Jan. 2014.
- [60] T. Liu *et al.*, "Non-convex tensor low-rank approximation for infrared small target detection," *IEEE Trans. Geosci. Remote Sens.*, vol. 60, pp. 1–18, Nov. 2022, Art. no. 5614718.
- [61] B. Li *et al.*, "Dense nested attention network for infrared small target detection," 2021, *arXiv:2106.00487*.
- [62] I. Reed, R. Gagliardi, and H. Shao, "Application of three-dimensional filtering to moving target detection," *IEEE Trans. Aerosp. Electron. Syst.*, vol. AES-19, no. 6, pp. 898–905, Nov. 1983.
- [63] N. J. Gordon, D. J. Salmond, and A. F. Smith, "Novel approach to nonlinear/non-gaussian Bayesian state estimation," *IEE Proc. F—Radar Signal Process.*, vol. 140, no. 2, pp. 107–113, 1993.
- [64] Z. Chen, M. Tian, Y. Bo, and X. Ling, "Improved infrared small target detection and tracking method based on new intelligence particle filter," *Comput. Intell.*, vol. 34, no. 3, pp. 917–938, 2018.
- [65] Z. Yu *et al.*, "Searching central difference convolutional networks for face anti-spoofing," in *Proc. IEEE Conf. Comput. Vis. Pattern Recognit.*, 2020, pp. 5295–5305.
- [66] Z. Su *et al.*, "Pixel difference networks for efficient edge detection," in *Proc. IEEE/CVF Int. Conf. Comput. Vis.*, 2021, pp. 5097–5107.
- [67] Y. Wang, X. Ying, L. Wang, J. Yang, W. An, and Y. Guo, "Symmetric parallax attention for stereo image super-resolution," in *Proc. IEEE Conf. Comput. Vis. Pattern Recognit. Workshops*, Jun. 2021, pp. 766–775.
- [68] C. Xiao *et al.*, "DSFNet: Dynamic and static fusion network for moving object detection in satellite videos," *IEEE Geosci. Remote Sens. Lett.*, vol. 19, pp. 1–5, 2022, Art. no. 3510405.
- [69] B. Hui *et al.*, "A dataset for infrared detection and tracking of dim-small aircraft targets under ground / air background," *China Sci. Data*, vol. 5, no. 3, pp. 291–302, 2020.
- [70] X. Sun *et al.*, "A dataset for small infrared moving target detection under clutter background," *Chin. Sci. Data*, 2021, doi: [10.11922/cs-data.2021.0015.zh](https://doi.org/10.11922/cs-data.2021.0015.zh).
- [71] J. Zhao *et al.*, "The 2nd Anti-UAV Workshop & Challenge," 2021. [Online]. Available: <https://anti-uav.github.io/>
- [72] D. P. Kingma and J. Ba, "Adam: A method for stochastic optimization," in *Proc. Int. Conf. Learn. Representations*, 2015.
- [73] N. Komodakis and S. Zagoruyko, "Paying more attention to attention: Improving the performance of convolutional neural networks via attention transfer," in *Proc. Int. Conf. Learn. Representations*, 2017.
- [74] A. Kappeler, S. Yoo, Q. Dai, and A. K. Katsaggelos, "Video super-resolution with convolutional neural networks," *IEEE Trans. Comput. Imag.*, vol. 2, no. 2, pp. 109–122, Jun. 2016.
- [75] J. Rivest and R. Fortin, "Detection of dim targets in digital infrared imagery by morphological image processing," *Opt. Eng.*, vol. 35, no. 7, pp. 1886–1893, 1996.
- [76] X. Zhang, Q. Ding, H. Luo, H. Bin, C. Zheng, and Z. Junchao, "Infrared dim target detection algorithm based on improved LCM," *Infrared Laser Eng.*, vol. 46, no. 7, pp. 726002–0726002, 2017.
- [77] Y. Lu, J. Valmadre, H. Wang, J. Kannala, M. Harandi, and P. Torr, "Devon: Deformable volume network for learning optical flow," in *Proc. IEEE Winter Conf. Appl. Comput. Vis.*, 2020, pp. 2705–2713.